The impact of realistic topographic representation on the parameterisation of oceanic lee wave energy flux

Lois Elizabeth Baker[1] and Ali Mashayek[1]

[1]Imperial College London

November 23, 2022

Abstract

Oceanic lee waves are generated when quasi-steady flows interact with rough topography at the bottom of the ocean, providing an important sink of energy and momentum from the mean flow and a source of turbulent kinetic energy. Linear theory with a spectral representation of topography is typically used to inform parameterisations of lee wave generation. Here, we use a realistic wave resolving simulation of the Drake Passage, a hot-spot of lee wave generation, to investigate the utility of such parameterisations for areas of complex large scale topography. The flow is often blocked and split by large amplitude topographic features, creating an 'effective topography', and calling into question the spectral representation of small scale topography for lee wave generation. By comparing the resolved modelled wave field to parameterisations employing various representations of topography, we show that spectral methods may not be appropriate in areas of rough topography. We develop a simple topographic representation consisting of an ensemble of topographic peaks, which allows physical treatment of flow blocking at finite amplitude topography. This method allows better prediction of bottom vertical velocities and lee wave energy flux than spectral methods, and implies that the nature of lee waves in such regions can be misrepresented by a spectral approach to topographic representation. This leads to both an overestimate of wave energy flux and an underestimate of wave nonlinearity, with implications for the mechanisms by which lee waves break and mix in the abyssal ocean.

The impact of realistic topographic representation on the parameterisation of oceanic lee wave energy flux

L. E. Baker[1] and A. Mashayek[1]

[1]Imperial College London, United Kingdom

Key Points:

- Typical lee wave estimates may overestimate wave energy flux and underestimate wave nonlinearity, with implications for how waves break
- Estimates can be improved by a topographic representation that allows flow blocking at individual features as opposed to spectral methods
- This can pave the way for implicit representation of topographic waves in non-wave-resolving climate models

Corresponding author: Lois Baker, `l.baker18@imperial.ac.uk`

Abstract

Oceanic lee waves are generated when quasi-steady flows interact with rough topography at the bottom of the ocean, providing an important sink of energy and momentum from the mean flow and a source of turbulent kinetic energy. Linear theory with a spectral representation of topography is typically used to inform parameterisations of lee wave generation. Here, we use a realistic wave resolving simulation of the Drake Passage, a hot-spot of lee wave generation, to investigate the utility of such parameterisations for areas of complex large scale topography. The flow is often blocked and split by large amplitude topographic features, creating an 'effective topography', and calling into question the spectral representation of small scale topography for lee wave generation. By comparing the resolved modelled wave field to parameterisations employing various representations of topography, we show that spectral methods may not be appropriate in areas of rough topography. We develop a simple topographic representation consisting of an ensemble of topographic peaks, which allows physical treatment of flow blocking at finite amplitude topography. This method allows better prediction of bottom vertical velocities and lee wave energy flux than spectral methods, and implies that the nature of lee waves in such regions can be misrepresented by a spectral approach to topographic representation. This leads to both an overestimate of wave energy flux and an underestimate of wave nonlinearity, with implications for the mechanisms by which lee waves break and mix in the abyssal ocean.

Plain Language Summary

Oceanic lee waves are generated when currents and eddies interact with rough sea-floor topography, and are important for causing turbulent mixing in the deep ocean when they break. Representing their effect in global models that cannot resolve them is challenging because estimates of wave generation depend on the sea-floor topography, which is not known at sufficient resolution globally, and is often too high for standard theories to apply. Here, we employ a novel method that better represents (compared to existing methods) the role of high resolution, rough, topography in inference of lee wave energy flux. Our study highlights the need for continuing efforts toward high-resolution mapping of the sea floor and is a step forward towards representing lee waves in coarse-resolution climate models.

1 Introduction

Oceanic lee waves are generated when quasi-steady stratified flow is disturbed by sea-floor topography, creating a vertically propagating wave that is phase locked to the generating topographic feature. Lee waves are known to be an important sink of energy from the eddying geostrophic flow, particularly in the Southern Ocean (SO), where they extract energy from the Antarctic Circumpolar Current (ACC) as it interacts with the rough topography (Nikurashin et al., 2012; Naveira Garabato et al., 2013; Yang et al., 2018). The energy in the lee wave field must then be redistributed, either back to the mean flow via wave-mean interactions, or to turbulent scales via a forward cascade, thus facilitating the transfer of energy from global scale wind- and buoyancy-forced currents to small-scale turbulent dissipation and mixing. Breaking internal waves are a major source of mixing in the interior ocean, allowing water mass transformation and sustaining the abyssal branch of the Meridional Overturning Circulation (MOC) (Wunsch & Ferrari, 2004; Mashayek, Salehipour, et al., 2017; MacKinnon et al., 2017; Whalen et al., 2020; Legg, 2021).

Occurring on horizontal scales of $O(1\text{ km - }10\text{ km})$ and vertical scales of $O(100\text{ m - }1\text{km})$, the full spectrum of lee waves is horizontally and vertically at the sub-grid-scale of even the most highly resolved global ocean models, and their effect on the oceanic buoyancy budget (through mixing) and momentum budget (through wave drag) must be parameterised. Previous work to estimate and parameterise lee wave energy flux in the ocean has been substantial. Most studies build upon the theoretical linear theory of (Bell, 1975), which, given some near-topography background flow speed and stratification, and some sufficiently small amplitude topography, allows the calculation of the linear wave perturbation fields and energy flux. Global estimates based on linear theory have estimated that the global energy flux into lee waves is between 0.15-0.75 TW, with over half occurring in the SO (Nikurashin & Ferrari, 2011; Scott et al., 2011; Trossman et al., 2013; Nikurashin et al., 2014; Wright et al., 2014). Parameterisations of lee wave driven mixing have been applied to ocean models using these estimated maps of wave generation by assuming that wave energy decays in the bottom few hundred metres of the ocean and inferring a corresponding turbulent diffusivity, showing that lee wave driven mixing has a significant impact on the ocean state and MOC through deep water mass transformation (Nikurashin & Ferrari, 2013; Melet et al., 2014; Broadbridge et al., 2016).

Comparisons of linear lee wave predictions to in-situ observations in the Southern Ocean have found that turbulent dissipation inferred from microstructure measurements could be up to an order of magnitude less than would be expected if all of the the estimated lee wave energy was dissipated in the deep ocean (Sheen et al., 2013; Waterman et al., 2013, 2014; Cusack et al., 2017; Voet et al., 2020). One possible source of this discrepancy is the assumption, made in theoretical estimates, that lee wave energy finds a local sink in turbulent dissipation and mixing due to wave breaking. Recent studies have suggested that this energy could instead propagate downstream and dissipate non-locally (Zheng & Nikurashin, 2019; Zheng et al., 2022), be reabsorbed into a sheared mean flow that decreases with height above bottom (Kunze & Lien, 2019), or interact with the upper ocean and reflect from the ocean surface (Baker & Mashayek, 2021). Another possible source of this discrepancy is that the generation estimates are too high. Trossman et al. (2015) compared several different lee wave parameterisations with observations in the Southern Ocean, and found high sensitivity to the representation of topography used.

The representation of topography for lee wave parameterisations is a large source of uncertainty for two primary reasons. Firstly, resolved bathymetric data at a sufficient resolution for lee wave generation is currently only available over around 20.6% of the ocean floor, where in-situ multi- or single-beam surveys have been carried out (GEBCO Bathymetric Compilation Group, 2021). Elsewhere, gravity-based bathymetric data derived from satellite altimetry has an effective resolution of approximately 6 km (Tozer et al., 2019). At lee wave generating scales of O(1 km - 10 km), the sea-floor is dominated by small-scale abyssal hills formed by volcanic and faulting processes at mid-ocean ridge spreading centres. Global estimates and many idealised simulations of lee wave generation have therefore used a statistical model of small-scale abyssal hills, proposed by Goff and Jordan (1988) (e.g. Nikurashin & Ferrari, 2011; Scott et al., 2011; Nikurashin et al., 2014; Klymak, 2018; Zheng & Nikurashin, 2019). Together with estimates of relevant topographic parameters, this model spectrum has been used to represent topography at lee wave-generating scales, assuming that larger scale topographic features are unimportant for lee wave generation.

However, even a full global knowledge of oceanic bathymetry at high resolution would not be sufficient to fully determine a topographic representation for lee wave generation. A second problem arises from the linearity assumption, that is, the necessary assumption for use of the linear theory that the characteristic height h of the topography is such that the topographic Froude number $Fr = Nh/U \ll 1$, where N and U are the buoyancy frequency and the flow speed near the sea-floor. For typical abyssal Southern Ocean values of $U \sim 0.1$ m s^{-1}, $N \sim 0.001$ s^{-1}, this requires that the characteristic topographic height is $\ll 100$ m - an assumption that is widely violated in the ocean. However, energetic arguments show that for a topographic feature taller than $\sim U/N$, the flow is unable to summit the obstacle, and is instead blocked at low levels, or splits and goes around the obstacle (R. B. Smith, 1989; Welch et al., 2001). The effective generating height of topography is therefore $h_{eff} \leq h_{cr} \sim U/N$, and this allows the linear theory to remain largely applicable to the real ocean. Idealised numerical studies using abyssal hill bathymetry at lee wave radiating scales with parameters representative of the Southern Ocean have verified the Bell (1975) linear theory with these finite amplitude corrections in 2D and 3D (Nikurashin & Ferrari, 2010a; Nikurashin et al., 2014).

Although small scale abyssal hills dominate oceanic bathymetry on lee wave generating scales, it has been noted that the larger scale bathymetry may also play a role in lee wave generation. Klymak (2018) showed, using idealised simulations, that the dissipative effects of large and small scale abyssal hill topography are coupled, and that flow acceleration due to larger scale topographic features can lead to changes in wave-generating horizontal scales, complicating the standard separation of scales for wave generation. It has also been noted that flow blocking at large scale topography can create an 'effective topography' with shorter horizontal scales than the original feature, allowing wave generation from topographic scales that would otherwise be deemed 'non-propagating' (e.g. Klymak et al., 2010; Cusack et al., 2017; Arbic et al., 2019; Perfect et al., 2020). The representation of topography is therefore inherently linked to the properties of the flow, which are themselves often modified by the large scale topography. It is the impact of realistic topography (including large scales and non-abyssal hill features) on lee wave generation estimates that is the focus of the current study.

Despite numerous idealised numerical studies of lee wave generation and parameterisation, there are few examples of lee wave studies with wave-resolving simulations using realistic bathymetry, due to computational constraints and difficulties in filtering wave fields in a realistic flow. There are however increasingly more wave resolving regional studies; de Marez et al. (2020), for example, compared high resolution simulations, linear theory, and surface lee wave signatures in satellite sun glitter images for lee wave generation from seamounts in the Gulf stream. It remains unclear, however, whether linear theory with statistical estimates of small scale abyssal hill topography can represent lee wave generation at realistic finite amplitude topography with a corresponding realistic eddying flow.

The aim of this study is to use a high resolution, wave resolving, regional simulation of the Drake Passage to investigate the nature of realistic lee wave generation, and compare linear lee wave parameterisations employing various representations of topography. The Drake Passage has been the focus of several numerical and observational studies of lee waves, largely due to its favourable conditions for lee wave generation; energetic mesoscale eddies of the ACC are funneled through the narrow gap between South America and the Antarctic peninsular, leading to high velocity bottom flows interacting with very rough topography including seamounts, ridges, and abyssal hills (e.g. Nikurashin & Ferrari, 2010a; Sheen et al., 2013; Cusack et al., 2017; Yang et al., 2018). We chose this study area for its high lee wave generation, its importance globally as a hot-spot for topographically enhanced mixing (St. Laurent et al., 2012; Merrifield et al., 2016; Mashayek, Ferrari, et al., 2017), for comparison to other lee wave studies and observations, and due to the relatively good coverage of multibeam bathymetry in the region, allowing a fairly realistic model bathymetry.

To investigate the nature of the realistic lee waves and the ability of lee wave parameterisations, we compare calculations (from the modelled resolved wave field) and estimates (parameterisations using the large scale model flow properties) of lee wave energy flux in the Drake Passage region. In each parameterisation, we use spatially low-pass filtered bottom velocities and stratification from the simulation, and vary the representation of topography. In particular, we compare *spectral* representations of topography, whereby following techniques used in standard oceanic lee wave estimates, the full topography is first truncated to lee wave generating scales before any corrections for non-linearity are applied, with a new *peaks* method, introduced here, which first accounts for flow blocking through the definition of an effective topography. The *peaks* method will be shown to represent local lee wave properties better than the *spectral* method, implying that in such regions, spectral topographic representation may misrepresent lee wave generation.

This paper is organised as follows. In §2, we recap the linear theory of Bell (1975), and discuss representation of topography for the lee wave problem, motivating the set of topographic representations to be used in our estimates. In §3 we describe our methods, including the realistic simulations (§3.1), corresponding wave filtering techniques (§3.2), and linear parameterisations (§3.3). In §4, we discuss our results, before summarising the findings of this study in §5 and discussing some of the caveats in §6. In §7, we consider some of the possible future directions of this work.

2 Theoretical Background

2.1 Linear theory

Lee waves are generated when flow interacts with bottom topography, perturbing the isopycnals and creating a disturbance that propagates vertically upwards and downstream in the frame of the topography. Linear theory is commonly used to estimate the wave field and generation rate. Under the assumption that there is some constant, uniform (or sufficiently slowly varying in time and space) background flow with horizontal velocity $\mathbf{U}$ and stratification N^2, and some characteristic topographic height h, the wave field can be treated as linear if the topographic Froude number $Fr = \frac{Nh}{|\mathbf{U}|} \ll 1$.

For $Fr \ll 1$, the wave quantities can be considered as small wavelike perturbations to the mean flow with horizontal wavenumber $\mathbf{k} = (k, l)$, vertical wavenumber m, and frequency ω. For this problem, application of a steady topographic boundary condition will later imply that the frequency ω in the frame of the topography vanishes, so for simplicity we set $\omega = 0$ hereafter. The Boussinesq, linearised equations of motion give the dispersion relation:

$$m^2 = |\mathbf{k}|^2 \frac{N^2 - (\mathbf{U}\cdot\mathbf{k})^2}{(\mathbf{U}\cdot\mathbf{k})^2 - f^2}\,, \tag{1}$$

where f is the Coriolis parameter. For typical oceanic conditions such that $N \gg |f|$, waves can only radiate vertically when m is real, that is when

$$|f| < |\mathbf{U}\cdot\mathbf{k}| < |N| \tag{2}$$

This limits the horizontal scale of propagating lee waves to a certain range. For typical parameters in the Southern Ocean $U \sim 0.1$ m s^{-1}, $N \sim 1 \times 10^{-3}$ s^{-1}, $f \sim 1 \times 10^{-4}$ s^{-1}, the range of wavelengths at which lee waves can be generated is ~ 600 m - 6 km.

Taking a linearised free-slip bottom boundary condition at the topography $h(x, y)$, and imposing a positive vertical group velocity (corresponding to upwards propagating waves with no internal or surface reflections) when m is real to determine its sign in Eq. (1), the horizontally averaged vertical energy flux is (Bell, 1975):

$$E = \overline{pw} = \frac{\rho_0}{4\pi^2}\int_{-\infty}^{\infty}\int_{-\infty}^{\infty} P(k,l)\frac{|\mathbf{U}\cdot\mathbf{k}|}{|\mathbf{k}|}\sqrt{(N^2 - \alpha(\mathbf{U}\cdot\mathbf{k})^2)((\mathbf{U}\cdot\mathbf{k})^2 - f^2)}\,dk\,dl\,, \tag{3}$$

where p and w are the pressure and vertical velocity perturbations, an overbar represents a spatial average, $P(k,l) \equiv \frac{1}{4L^2}|\hat{h}(k,l)|^2$ is the topographic power spectrum, with $\hat{h}(k,l)$ the Fourier transform of the topography $h(x,y)$, and $4L^2$ is the area over which $h(x,y)$ is defined. We have also introduced a parameter $\alpha \in \{0, 1\}$ which is equal to 1 unless the hydrostatic approximation is made, in which case $\alpha = 0$. When $|\mathbf{U}\cdot\mathbf{k}|$ is outside of the radiating range in Eq. (2), the sign of m (c.f. Eq. (1)) must be taken so that disturbances are vertically exponentially decaying, which leads to a choice of branch of the square root in Eq. (3) such that integrand is odd in k, l, and therefore only radiating wavenumbers contribute to the integral. Note that real topography $h(x, y)$ implies that $P(k, l)$ is an even function in k, l.

The energy flux E can also be expressed in terms of the Eliassen-Palm (E-P) flux $\mathbf{F}$ (Eliassen & Palm, 1960) as:

$$E = \overline{pw} = -\rho_0 \mathbf{U} \cdot \mathbf{F} \tag{4}$$

where

$$\mathbf{F} = \begin{pmatrix} \overline{uw} - f\overline{vb}/N^2 \\ \overline{vw} + f\overline{ub}/N^2 \end{pmatrix} \tag{5}$$

where $\mathbf{u} = (u, v, w)$ are the wave velocities, and b is the wave buoyancy. It is the E-P flux that is conserved with wave propagation in the absence of energy loss to dissipation and mixing, rather than the vertical flux of horizontal momentum $(\overline{uw}, \overline{vw})$. The extra contribution $(-f\overline{vb}/N^2, f\overline{ub}/N^2)$ to Eq. (5) represents the horizontal force exerted on particles on a wavy surface due to rotation (Bretherton, 1969). If $\mathbf{U}$ varies with the vertical coordinate z, the energy flux E increases/decreases with $\mathbf{U}$ as waves interact with the sheared mean flow (Eliassen & Palm, 1960). Here, however, we focus on bottom generation of waves and assume that near the seafloor both $\mathbf{U}$ and N are sufficiently uniform in the vertical for their gradients to have no impact on wave generation. This may not be justifiable everywhere, but is a widely used assumption, and investigation of its impact is not the focus of the current study.

2.2 Representation of topography

When $Fr \ll 1$, the linear theory is formally valid, and the power spectrum $P(k, l)$ can be found in a straightforward way from the Fourier transform of the topography $h(x, y)$. However, as discussed in the introduction, there exist two main problems with finding P for use in global lee wave parameterisations.

Firstly, knowledge of the oceanic bathymetry at sufficient resolution for lee wave generation globally does not exist. Bathymetric data, the most up to date of which is compiled into the General Bathymetric Chart of the Oceans (GEBCO Bathymetric Compilation Group, 2021, hereafter GEBCO), consists of data from multiple sources, including direct methods such as shipboard single- and multibeam echo soundings, and indirect methods such as predictions based on satellite-derived gravity data. Of these, only multibeam data collected in swathes several kilometres wide by in-situ research vessels is sufficiently resolved to represent 3D lee wave generating scales of $O(1 \text{ km - } 10 \text{ km})$. Some regions of active oceanographic research, such as the Drake Passage, now have relatively good multibeam coverage. Due to the sparse multibeam coverage in the global ocean, estimates of lee wave generation generally employ the theoretical Goff and Jordan (1988) von Kármán model of small scale abyssal hill topography, which is a statistical description of topography on $\mathcal{O}(0.1-50 \text{ km})$ scales derived from ridge-crest processes, off-ridge tectonics, and vulcanism. The topographic power spectrum is given by

$$P_{GJ}(k, l) = \frac{4\pi\overline{h^2}\nu}{k_n k_s} \left(1 + \frac{|\mathbf{k}|^2}{k_n^2}\cos^2(\theta - \theta_s) + \frac{|\mathbf{k}|^2}{k_s^2}\sin^2(\theta - \theta_s)\right)^{-(\nu+1)}, \tag{6}$$

where $\overline{h^2}$ is the root-mean-square (RMS) topographic height, k_s is the characteristic wavenumber in the strike direction (direction of longest variation), k_n is the characteristic wavenumber in the cross-strike direction, ν determines the steepness of the spectrum, and θ_s is the angle of the strike direction, measured from north (Scott et al., 2011). Several global estimates of these parameters have been made, based upon different data sources. Goff (2010, 2020) used statistical properties of abyssal hills to relate smaller scales to the satellite altimetry based gravity field. Goff and Arbic (2010) made an almost independent estimate, based upon statistical relationships between the seafloor spreading rate and direction. These two datasets are explained in detail in Scott et al. (2011), wherein the global lee wave flux is calculated for each. Note that bathymetric features other than abyssal hills, for example volcanic seamounts, mid-ocean ridges, and continental margins are purposefully excluded from these estimates of topographic parameters.

Another independent estimate of the topographic parameters for the purpose of estimating lee wave generation was made by Nikurashin and Ferrari (2011). Using a simplified and isotropic version of Eq. (6), they estimated the topographic spectrum globally on a 3° by 3° grid using $\sim 200,000$ available single beam segments of ship-board bathymetry. The use of this dataset did not exclude the contribution of non-abyssal hill bathymetry in the same way as the Goff (2010) spectrum, although topographic parameters were derived via a fit to the simplified version of Eq. (6) in the 2 - 20 km wavelength range only. Nikurashin and Ferrari (2011) argued that the isotropic assumption in their estimate was unimportant, since the flow is dominated by eddies that impinge on the topography from all angles. However, Trossman et al. (2015) showed that adding information about anisotropy to lee wave closures can bring estimates for energy dissipation closer to observations. Yang et al. (2018) showed, using an isotropic version of the Goff (2010) topographic parameters, that assuming isotropy can cause a 40% overestimation of energy flux in the SO, or 43% in the Drake Passage, implying that the flow direction is correlated with the bathymetry in the region.

Comprehensive sensitivity studies of energy flux resulting from the Goff (2010); Goff and Arbic (2010) and Nikurashin and Ferrari (2011) sets of topographic parameters found moderate differences between the various realisations, especially when isotropy is assumed (Scott et al., 2011; Trossman et al., 2015; Yang et al., 2018). The Goff (2010) dataset is considered to be superior to the Goff and Arbic (2010) dataset in its treatment of sedimentation, and due to its observational basis (Scott et al., 2011). Having a directional velocity field from our simulations, we do not need to use an isotropic assumption, which may lead to an overestimate of energy flux (Yang et al., 2018; Trossman et al., 2015). We therefore use the Goff (2010) topographic parameters as our abyssal hill estimate (labelled *G2010*), explained further in §3.3.3.

The second problem with topographic representation for linear lee wave calculation is the finite amplitude of sea-floor topography. Realistic oceanic topography varies on large scales, with ridges up to several kilometres in height (e.g. figures 2b,c), implying topographic Froude numbers of up to $O(10)$, well outside of the necessary limit $Fr \ll 1$ for application of the linear theory. However, when flow encounters a topographic feature, energetic arguments show that it cannot vertically rise a distance of greater than $\sim U/N$ (R. B. Smith, 1989; Welch et al., 2001). Blocking or splitting must then occur for obstacles with $Fr \gtrsim 1$, whereby the flow is blocked at low levels or goes around the obstacle. This creates an 'effective topography', with only the 'cap' of a topographic feature generating waves. The effective Froude number is then always $Fr_{\text{eff}} \lesssim Fr_C \sim O(1)$, where the exact critical value Fr_C depends on the shape and aspect ratio of the topography and characteristics of the flow (Eckermann et al., 2010; Perfect et al., 2020). Therefore, with a modified representation of topography, linear theory can be expected to apply more widely than a standard definition of the Froude number would suggest.

Since lee waves cannot be generated at large scales such that $|\mathbf{U}\cdot\mathbf{k}| < |f|$ or small scales such that $|\mathbf{U}\cdot\mathbf{k}| > |N|$, the spectrum $P(k,l)$ is effectively truncated in Eq. (3) to include only the wave generating scales. This also has the effect of lessening the characteristic height of the effective topography represented in the energy flux calculation (Eq. (3)), reducing (or hiding) issues with nonlinearity. Where the RMS height of the topography is such that $Fr \gtrsim 1$, blocking and splitting means that there is a critical Froude number Fr_c above which the energy flux saturates. Idealised simulations with abyssal hill topography truncated to the radiating range (Eq. (2)) and defined as in Eq. (6) show that the $Fr_c = 0.7$ for 1D topography, and 0.4 for 2D topography (Nikurashin & Ferrari, 2010a; Nikurashin et al., 2014). To take this effect into account, the energy flux E (or equivalently, the RMS topographic height) can be corrected using a multiplying factor (e.g. Nikurashin & Ferrari, 2010a; Scott et al., 2011):

$$E_{\text{corrected}} = \begin{cases} E\,, & Fr \le Fr_c \\ \left(\frac{Fr_c}{Fr}\right)^2 E\,, & Fr > Fr_c\,. \end{cases} \tag{7}$$

However, although the effect of blocking on the energy flux can be dealt with empirically by this correction factor, there remain issues associated with the representation of topography (Trossman et al., 2013; R. B. Smith & Kruse, 2018). Consider some full topography, whether that is derived from an untruncated synthetic spectrum $P(k,l)$, or 'actual' bathymetric data. This topography then contains both large and small scales, and will likely be highly 'nonlinear' in the sense that its characteristic height will be much larger than U/N. The 'effective' topography seen by the flow (termed a lowest over-topping streamline, or LOTS by Arbic et al. (2019)) will then consist of a collection of isolated 'caps' of height $O(U/N)$, along with some unaltered small scale topographic features. However, if instead the large scales are first removed from the topography by truncating the spectrum with some estimate of bottom U and N so that $|f| < |Uk| < |N|$, the 'effective topography' may be significantly different. In particular, removal of smaller topographic wavenumbers can introduce peaks where there were none before.

Figures 1a,b show two example large scale topographies where there are significant differences between these two representations. In figure 1a, an idealised sinusoidal large scale topography is shown in black. It has wavelength outside of the radiating range, thus if the non-propagating scales are first removed via a spectral decomposition (we hereafter term this the *spectral* method), it becomes zero and no waves are generated. If instead, the cap approximation is used, then the effective topography (in blue) consists of several peaks with $Fr \simeq 1$, which will generate nonlinear and horizontally isolated waves. This effective topography with non-radiating scales removed is shown in green. The energy flux found using the *spectral* method will therefore be underestimated. In figure 1b, the idealised large scale topography is an isolated Gaussian (shown in black). If the non-propagating scales are removed, the spectral decomposition still contains the smaller wavelengths, and thus the resulting topography gains several peaks (shown in blue). These peaks would result in wave generation in the energy flux calculation, perhaps nonlinear themselves. However, the effective topography (shown in red) consists of just one isolated peak. This effective topography with non-radiating scales removed is shown in green. In this case, the energy flux would likely be overestimated by the *spectral* method.

These idealised topographies demonstrate how using the full topography in the expression (3), and thereby truncating the spectrum before any other corrections for finite amplitude, could poorly represent the actual nature of the wave field. By this argument the fluxes can be both over- and under-estimated in areas of large scale topography.

Blocking of the large scale flow and its connection to lee wave energy flux has been recognised to be important in both the ocean and the atmosphere. Parameterisation of lee wave (mountain wave) drag in atmospheric models has received much attention, dating from the 1940s (e.g. Queney, 1948), and reviewed in Wurtele (1996); Teixeira (2014); R. B. Smith (2019). Indeed, much of the theory is identical, and oceanic lee wave studies often build upon the pre-existing atmospheric literature, although the primary focus of such studies is often wave drag, rather than both drag and the more oceanically relevant energy dissipation and mixing. The representation of topography in atmospheric models does not suffer from the first problem discussed above - the global land elevation dataset is sufficiently well resolved (Elvidge et al., 2019). Due to the larger horizontal scales of atmospheric than oceanic lee waves, modern global atmospheric models with horizontal grid resolution of $O(10\text{ km})$ do resolve larger mountain waves, but the effect of sub-grid-scale orography must still be parameterised (Vosper et al., 2020). Thus, the second issue of nonlinearity and dealing with topographic blocking at complex sub-grid-scale topography remains (R. B. Smith & Kruse, 2018; Elvidge et al., 2019).

The Garner (2005) scheme helps to solve this problem by building upon a linear analytic drag based on the power spectrum of topography (similar to that of Bell (1975)) by splitting this drag into a propagating (wave) and non-propagating (blocked) part. The sub-grid-scale topography is represented as an ensemble of individual topographic features, with properties (such as height, areal extent, and aspect ratio) given by statisti-

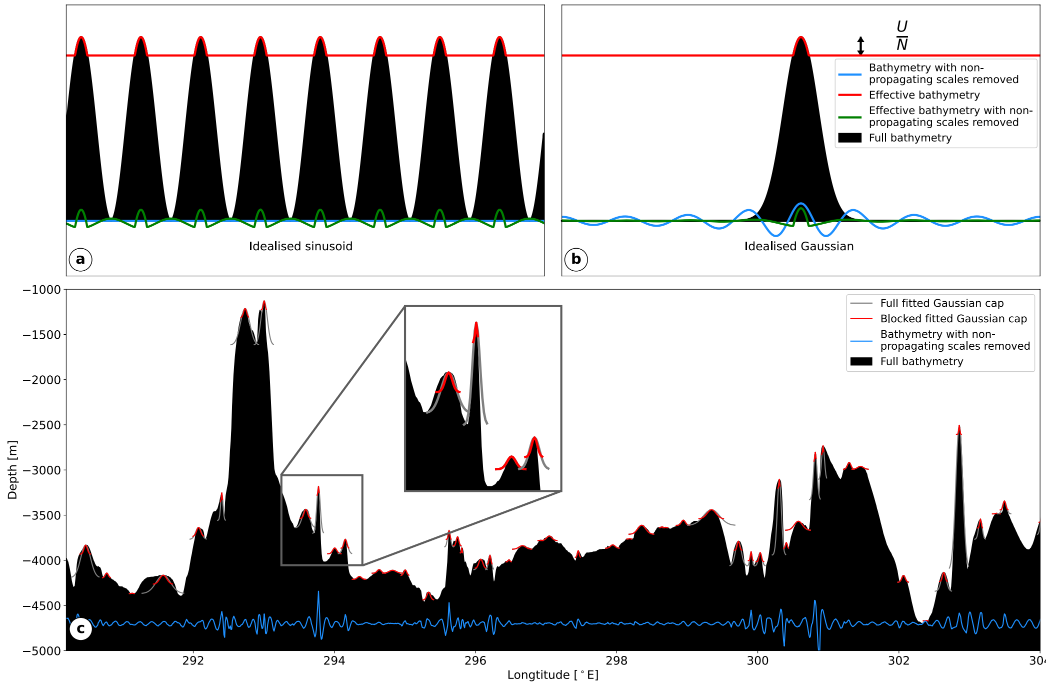

Figure 1. Schematic of idealised 1D (a) sinusoidal and (b) Gaussian topography, showing the effect of truncation to small (wave generating) scales on the full (black) and effective (red) topography. (c) Section of Drake Passage bathymetry used in the model at -57°N demonstrating (a 1D version of) the *SS:peaks* method. First, 1D Gaussian curves (grey) are fitted to each peak. Then, blocked peaks (red) are found (here with a blocked height of $U/N = 100$m) to represent the effective topography. The full topography high passed filtered at wavenumber $k = f/U = 1.2 \times 10^{-3}$ is shown in blue.

cal parameters at the grid-cell level. Consideration of individual features allows the separation of drag due to the blocked flow, and wave drag from the cap of the feature. Trossman et al. (2013) applied the Garner (2005) and Bell (1975) parameterisations to both an offline and online ocean model using the Goff and Jordan (1988) abyssal hill spectrum with Goff (2010) topographic parameters, finding similar inferred energy dissipation rates from wave drag in each, with some spatial differences. It is noted that the Garner (2005) scheme does not explicitly account for rotation in the formulation of the drag, which is important for the truncation of lee wave generating scales in the ocean. The choice of parameters for the finite amplitude sub-grid-scale topography is also a source of uncertainty (Garner, 2005). In current operational atmospheric models such as the Met Office Unified Model (UM), a similar scheme (Lott, 1998) is used, with sub-gridscale orography represented by statistical parameters (Elvidge et al., 2019).

A method developed in this study (termed the *peaks* method) for prediction of energy flux at blocked topography uses similar physical ideas to the Garner (2005) scheme. However, we focus on a simple local representation of actual bathymetric features, rather than using a statistical representation at a grid-cell level. We also focus on the wave fields only, leaving the important treatment of non-propagating scales to future studies. This allows us to more clearly elucidate the nature of the wave field at any location in our domain, and to eliminate some of the statistical parameters needed in a complex drag parameterisation such as the Garner (2005) scheme.

Differences in the nature of wave generation by a spectral abyssal hill topography, and by a blocked flow, which sees only 'caps' of rough topography, may be significant (Arbic et al., 2019). Whilst waves generated by a periodic topography are not expected to overturn and break (Baines, 1995; Welch et al., 2001), flow over isolated obstacles (or mountains) can cause convective wave breaking, hydraulic jumps, and down-slope windstorms which dramatically increase the wave drag (e.g. Peltier & Clark, 1979; Durran, 1986). The latter case has been extensively studied in an atmospheric context, but less so in an oceanic context, perhaps partly due to the common (and necessary) abyssal hill representation of oceanic bathymetry. A further difference between atmospheric and oceanic lee wave generation is the range of scales at which it can occur - the upper horizontal wavelength $2\pi U/f$ of wave generation is significantly larger for the atmosphere than the ocean, since atmospheric winds are faster than oceanic currents. Isolated mountain ranges on land that have been the subject of numerous atmospheric lee wave studies are therefore less relevant to the oceanic lee wave picture. However, this large scale topography may still play an important role by inducing energetic and nonlinear wave breaking at its 'cap', with reduced effective width.

A key property of an 'effective topography' in areas susceptible to flow blocking and splitting is that it varies with the flow itself. If U is enhanced locally at some blocked topography, the effective topography will become taller, since it scales with U/N. Thus, the energy flux does not increase as U^2 as it would with some fixed topography (see Eq. (3)), but instead as U^4, neglecting changes to the effective width of the topography (Voisin, 2007; Perfect et al., 2020), or U^3, assuming a fixed topographic aspect ratio (Legg, 2021). For this reason, temporal and spatial resolution of bottom velocities is expected to be important in accurately estimating lee wave energy flux, especially in regions with high Froude number. Small regions of high velocities, perhaps enhanced by flow interaction with the larger scale topography, can disproportionately contribute to a spatially averaged energy flux.

In this study, we investigate the impact of different topographic representations on lee wave energy flux in the Drake Passage domain, which consists of areas of abyssal hill topography, large ridges, and seamounts. The bathymetry used in the model is from the Smith and Sandwell (1997, v15.1) 1 minute product, and contains some areas of multibeam topography alongside satellite altimetry derived estimates of the bathymetry. It is therefore incomplete in terms of coverage of lee wave generating scales, and we later investigate the impact of an updated multibeam bathymetry to the estimates in the region.

The calculations of energy flux made in this study are listed in Table 1. Two estimates of lee wave generation are first made from the resolved wave field in the simulations. Separating the wave field from the numerous other processes in these realistic simulations is not straightforward due to the stationary nature of the lee waves, which vary on the same timescale as their generating flow. We consider two different methods; first a directional spatial filter, which we introduce in this work and refer to as *spatial filter*, then a recent open source Lagrangian filtering package developed by Shakespeare et al. (2021) to extract internal waves from other processes, referred to as *Lagrangian filter*.

We then make two estimates of lee wave generation using the linear theory applied to the bathymetry used in the model to attempt to exactly replicate the simulated lee wave generation. The first, *SS:spectral*, represents the lee wave generating scales of the Smith and Sandwell (1997, v15.1) bathymetry used in the model through a spectral representation, which suffers from an inability to properly represent large scales and blocking. The second, *SS:peaks*, determines the peaks which can generate lee waves, representing them as 1D Gaussian bumps, and performs the energy flux calculation for each individually - thereby allowing explicit blocking/splitting of flow. This is intended to represent wave generation from the multi-scale topography of the region in a more phys-

Table 1. Calculations of energy flux in the Drake Passage region

Type	Calculation	Description
Estimation from resolved wave field in simulation	*Spatial filter*	Directional spatially filtered wave fields from simulation
	Lagrangian filter	Lagrangian filtered wave fields from simulation
Parameterisation using large scale flow from simulation	*SS:spectral*	Linear theory with topographic spectrum derived from the Smith and Sandwell (1997, v15.1) bathymetry used in the simulation.
	SS:peaks	Linear theory with our *peaks* method, derived from the Smith and Sandwell (1997, v15.1) bathymetry used in simulation.
	GEBCO:spectral	Linear theory with topographic spectrum derived from GEBCO bathymetry.
	GEBCO:peaks	Linear theory with our *peaks* method, derived from GEBCO bathymetry.
	G2010	Linear theory with Goff and Jordan (1988) abyssal hill spectrum and Goff (2010) topographic parameters.

ically consistent way. The comparison of these parameterisations with the model wave generation begins to address the second topographic representation problem discussed above - if we know some complex bathymetry and flow, how well can we predict lee wave generation?

Recognising that the bathymetry used in the model (interpolated to 0.01° horizontal resolution from the one minute Smith and Sandwell (1997, v15.1) product) is limited by model resolution and has been continuously improved by additions of multi-beam data and improved satellite altimetry in recent years since our model development began, we also apply the methods of *SS:spectral* and *SS:peaks* to the latest and higher resolution 15 arc second GEBCO 2021 dataset, which has multibeam coverage of 70% of our domain. These two estimates are labelled *GEBCO:spectral* and *GEBCO:peaks*, and allow us to move closer to a 'real' energy flux in the Drake Passage region.

The final estimate *G2010* also employs the linear theory, but now with bathymetry represented by estimates of abyssal hill spectra, taking into account unresolved bathymetry and with applicability to global scale parameterisations. We use the Goff and Jordan (1988) spectrum, with topographic parameters from Goff (2010, 2020); Scott et al. (2011). As stated before, this estimate purposefully excludes other topographic forms such as ridges and seamounts, and although containing more smaller scale bathymetry, may therefore underestimate the energy flux if these larger scales contribute significantly to lee wave energy flux. The consideration of the abyssal hill and multibeam GEBCO bathymetries allows us to address the first topographic representation problem discussed above - if we don't know the real bathymetry, how well can we approximate it using statistical estimates?

3 Methods

3.1 Numerical Model

We use a realistic, wave-resolving model of the Drake Passage to investigate the wave generation in the region, based on a similar model described in Mashayek, Ferrari, et al. (2017). The simulation is performed at 0.01° horizontal resolution using the hydrostatic configuration of the Massachusetts Institute of Technology general circulation model (MITgcm, Marshall1997).

There are 225 vertical levels, with resolution dz varying smoothly from $dz = 10$ m at the surface to $dz = 25$ m at 600 m depth, $dz = 25$ m between 600 m and 4555 m depth, and varying smoothly from $dz = 25$ m to 62 m at the maximum depth of 5660 m. This resolution is increased from the simulation described in Mashayek, Ferrari, et al. (2017), and allows better resolution of the internal wave field.

The model is nested within a model of larger region of the SO described in Tulloch et al. (2014), and the initial and boundary conditions are derived from this parent simulation, also performed using the MITgcm; this nesting is shown in figure 2a. The parent simulation was forced at the open boundaries by restoring velocity, temperature and salinity to the Ocean Comprehensive Atlas (OCCA), an 18 month long ocean state estimate (Forget, 2010), and at the surface by near surface air temperature, wind speed, precipitation, humidity, long and short wave radiation from the ECMWF ERA-Interim reanalysis product (Simmons et al., 2006). The nested simulation uses the same surface forcing, with a fully nonlinear free surface, and open boundary conditions derived from the parent simulation are used at four boundaries for sea surface height, potential temperature, salinity, meridional and zonal velocities. In addition, a restoring boundary condition creates a sponge layer of 1 degree thickness in which the potential temperature, salinity, zonal and meridional velocities are relaxed to the parent simulation on a timescale of 4 hours at the boundary, with the relaxation vanishing at the inner edge of the sponge layer. The sponge layer is removed for analysis purposes.

The vertical diffusivity and viscosity have background values of 5×10^{-5} m^2 s^{-1}, and are enhanced by the K-profile parameterisation (KPP) with the critical Richardson number for shear instability set to $Ri_c = 0.3$ (Large et al., 1994). Horizontal viscosity is implemented through the biharmonic Leith scheme with a coefficient of 2 (Leith, 1996; Fox-Kemper & Menemenlis, 2008). Quadratic bottom drag with a coefficient of 2.5×10^{-3} is used, and the bathymetry is interpolated from the Smith and Sandwell (1997, v15.1) one minute product.

The simulation starts in July, and is integrated for 100 days with a timestep of 24 s. We use the final 30 days of the simulation (early September to early October) for our analyses.

Although the model is lee wave resolving and realistic, as with any numerical model there are uncertainties. The model does not include tides, which, although making it less realistic, does allow us to more easily isolate the lee wave generation. However, it has been suggested that the generation of internal tides in the Drake Passage could modify lee wave generation (Shakespeare, 2020). The hydrostaticity of the model is necessary due to limitation of computational resources, and may impact the lee wave field. Hydrostaticity is a common assumption for lee wave generation (e.g. Trossman et al., 2013; Klymak, 2018) but can affect the wave field (F. T. Mayer & Fringer, 2020). We investigate the impact of the hydrostatic assumption on the wave parameterisations in §4.4. As previously mentioned, the bathymetry used in the model does not have full resolution multi-beam data everywhere, and is therefore likely to generate less energy flux than the real bathymetry in the region. The model resolution, at 0.01°, certainly resolves the larger and most energetic waves, but may not permit the full spectrum - this is discussed in §4.4. Finally, such models suffer from their inability to properly represent sub-grid-

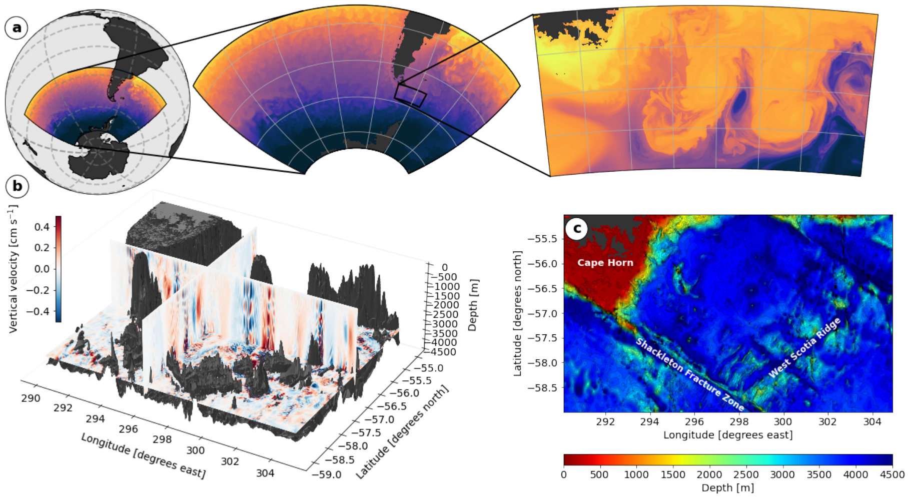

Figure 2. (a) A nesting diagram for the Drake Passage regional model. Sea surface temperature is shown. (b) The full model domain, showing bathymetry and slices of daily averaged vertical velocity. Lee waves can be seen propagating from the topography vertically to the surface. (c) Smith and Sandwell (1997, v15.1) bathymetry used in the model, with some major topographic features labelled.

scale wave breaking. Parameterisations for horizontal viscosity (here, the Leith biharmonic scheme) and vertical viscosity and diffusivity (here, the KPP scheme), are widely used in such models, but their applicability when waves are partially or fully resolved is not certain (Fox-Kemper & Menemenlis, 2008). However, the focus of this study is wave generation, and although the model parameterisation of wave decay through mixing and dissipation will certainly impact our estimates of energy flux (e.g. see figure 5c), and must be considered, it is not our focus here and does not impact our main findings.

3.2 Wave filtering

The flow field of the simulations is complex and energetic. Mesoscale eddies with horizontal velocities of $\mathcal{O}(0.1 - 1 \text{ ms}^{-1})$ interact with the rough topography, creating smaller scale wake vortices, non-propagating processes, and lee waves (see figure 2b). A wealth of submesoscale structures develop in the upper ocean, and near-inertial waves (NIWs) propagate downwards from the surface and upwards from the topography, although we note that the model's 6 hourly wind forcing is not sufficiently frequent to force a full NIW field. The lee wave field spans the entire water column, with waves generated at the bottom topography propagating to the upper ocean, interacting with the flow structures there, and reflecting back downwards, as discussed in Baker and Mashayek (2021). This multitude of processes on various temporal and spatial scales leads to substantial difficulties in identifying and isolating the lee wave field.

We compare two different methods of filtering the lee wave field from the rest of the flow. The *spatial filter* is a directional spatial filter developed in this work, and the *Lagrangian filter* uses the recent Lagrangian filtering method developed by Shakespeare et al. (2021). In both cases, to directly calculate the energy flux, the correlation of pressure and vertical velocity $\overline{pw}$ must be found. However, when filtering the simulation output fields, we found pressure difficult to work with given the large relative size of the background to perturbation fields. We instead use the relation (4) to infer the energy flux from the perturbation fields of the velocities and buoyancy, together with spatial 20 km low-pass filtered background fields U,V and N.

3.2.1 Spatial directional filter

The stationary nature of lee waves in the reference frame of the topography means that temporal filtering to separate lee waves from the mean flow is not appropriate. The stationarity of the lee wave field does, however, allow us to perform a low pass temporal filter to remove higher frequency structures, as in de Marez et al. (2020). We do this by simply using daily average output fields. This timescale was chosen to retain as much of the lee wave signal (which varies on the timescale of the mean flow) as possible whilst filtering out faster motions such as NIWs, which have a period near 14 hours.

Having filtered out the high-frequency signal, we must then remove the low frequency, large spatial scale signal of the mean eddying flow. Most lee waves in this region are generated with horizontal wavelengths of less than 20 km, which corresponds to generating flows of less than $\sim 0.4\text{ms}^{-1}$. Therefore, after applying a high pass spatial filter to the output fields at 20 km, the lee waves remain. However, so do many other small scale structures, especially near topography and the surface. We therefore develop a novel second filtering step, whereby we make use of the observation that lee wave crests are generally perpendicular to the background flow direction (neglecting 3D effects and changes in flow direction with height), whereas other filament type structures that we wish to filter out often have structures aligned with the mean flow. We therefore use a spatial directional filter (*spatial filter*) to perform a 1D high pass filter with cut-off 20 km along the mean flow direction only. This is similar to the method employed by Goff (2010) to separate abyssal hill bathymetry from fracture zones. Full details are given in Appendix A.

We find that this method is relatively successful, although can be inaccurate close to topography. Results are compared with the Lagrangian filtering method in §4.2.

3.2.2 Lagrangian filter

Shakespeare et al. (2021) recently presented a new open source implementation of Lagrangian filtering, which allows internal waves in a high resolution simulation such as our own to be temporally filtered in a frame of reference moving with the flow. Internal waves with frequency ω in the rest frame have frequency $\Omega = \omega - \mathbf{U}\cdot\mathbf{k}$ in the frame of the flow due to Doppler shifting. All internal waves satisfy $\Omega^2 \geq f^2$, and a temporal filter in the frame of the flow with cut-off frequency f thereby allows internal waves to be separated from the non-wavelike flow. Note that lee waves are a special case where $\omega = 0$.

This package allows us to easily isolate the internal wave field. The method was found by Shakespeare et al. (2021) to be effective at filtering lee waves from a mean flow when tested against a similar realistic simulation to our own, which also used MITgcm. Hourly average input fields were used, and a filtering window of width ± 1 day was found to give only a 1% RMS error compared to a filtering window of ± 2.4 days.

We replicate their calculation with our own hourly average simulation fields. An example of the *Lagrangian filter* method is shown in figure 3, with hourly averaged zonal (top) and vertical (bottom) velocity slices shown in figures 3a,c, and their corresponding filtered wave field in figures 3b,d. In the full zonal velocity field (figure 3a), large scale eddies are visible, along with some enhancement of large scale flow towards the topography. While some wave field is evident in figure 3a, it becomes much clearer when filtered in figure 3b - note the change in colour scale. Wavelike structures are visible throughout the water column, corresponding to both top- and bottom- generated waves. Wave zonal velocity perturbations exceed 5 cm s^{-1} in some areas, especially near topography. In contrast to the clear difference between the full and filtered zonal velocity fields, the

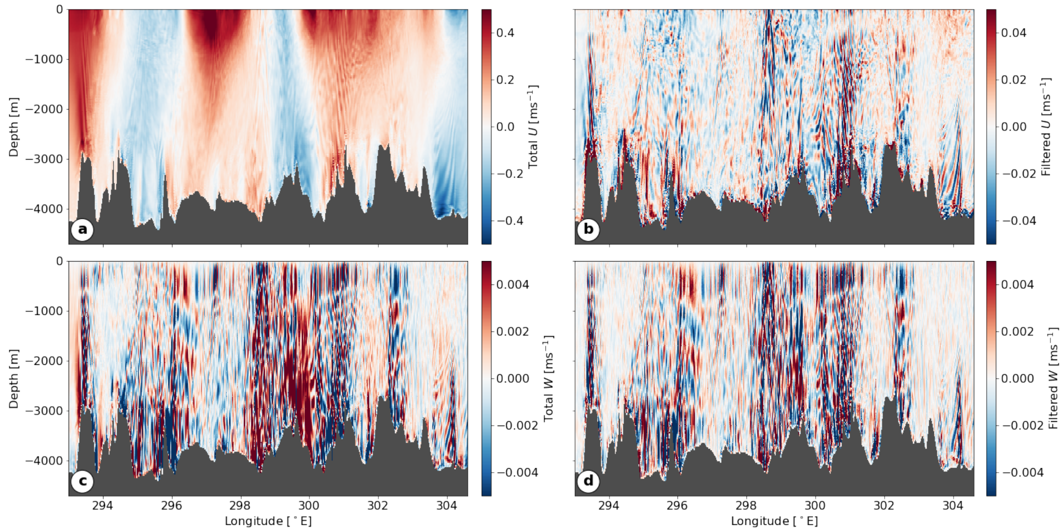

Figure 3. Demonstration of the *Lagrangian filter* process. (a) Hourly averaged zonal velocity U, (b) corresponding Lagrangian filtered zonal velocity, (c) Hourly averaged vertical velocity W, and (d) corresponding Lagrangian filtered vertical velocity, all at -57.5° N

vertical velocity field appears largely unchanged, although some larger scale structures are removed. The lee waves show reflection from the ocean surface, as reported in Baker and Mashayek (2021). Note that the higher wave vertical velocities and lower wave horizontal velocities near the surface are predicted by lee wave theory in a varying background flow when N decreases, as it does here in the near surface mixed layer (Baker & Mashayek, 2021).

A disadvantage of this method for our purposes is its inability to distinguish between lee waves and other varieties of internal waves. In this simulation, downwards propagating NIWs are generated at the surface, and upwards propagating NIWs are generated near topography. This is consistent with the mechanism suggested by Nikurashin and Ferrari (2010b) of deposition of lee wave energy into inertial oscillations, leading via parametric instability to the formation of NIWs, which provide a vertical shear that further facilitates lee wave breaking. It is therefore likely that our lee wave energy flux estimates will be contaminated by NIWs. Bottom generation rather than upper ocean lee wave flux is our focus here, so we do not expect the reduction of energy flux by downwards propagating, surface generated, NIWs to affect our calculations significantly. Near topography, if NIWs are fed by breaking lee waves as suggested by Nikurashin and Ferrari (2010b), upwards energy flux in the abyssal ocean containing both a NIW and lee wave contribution could be considered to be a closer estimate to the true lee wave generation. Given the uncertainties involved with the breaking and dissipation of lee waves near topography in this simulation, we will not further consider the role of NIWs here, but this will be the topic of future work.

We perform the Lagrangian filtering for our 3D domain for one time step during day 25 of the 30 day output. The energy is then calculated via the E-P flux from the filtered wave fields as in Eqs. (4)-(5). The horizontal average (represented by the overbar in Eq. (5)) at each location is calculated over a 20 km by 20 km box. The results are compared to the *spatial filter* method in §4.2.

3.3 Linear Parameterisations

For each of our parameterisations (listed in Table 1), we use daily averages of velocity and stratification from the simulation, averaged over the bottom 500 m. Estimating the establishment time T for lee waves as the time taken for (hydrostatic, non-rotating, two-dimensional) waves to propagate one vertical wavelength gives $T \sim 2\pi/|Uk|$ (Klymak & Legg, 2010). Since $|Uk| > |f|$ for propagating lee waves, this gives $T \lesssim 14$ hours, and we expect that daily averaged fields are sufficiently low-frequency to represent a background flow. The choice of 500 m is consistent with a typical lee wave vertical wavelength and with the choice of Nikurashin and Ferrari (2011); Yang et al. (2018).

Each parameterisation can be made with or without the hydrostatic approximation by changing the value of α in Eq. (3). Since our simulations are hydrostatic, for the best comparison we will use the hydrostatic approximation in the linear parameterisations unless otherwise stated - the impact of this will be shown in figures 9 and 10.

3.3.1 The spectral method

This method is applied to both the model's Smith and Sandwell (1997, v15.1) bathymetry (*SS:spectral*) and the GEBCO bathymetry (*GEBCO:spectral*). We represent bathymetry at longitude x and latitude y by a topographic spectrum $P(k, l; x, y)$, found at each simulation grid point using a sliding window Fourier transform. For details of the calculation, see Appendix B.

Once the topographic spectrum $P(k, l; x, y)$ has been found, the energy flux at (x, y) is found from Eq. (3) using the model velocities (U, V) and buoyancy frequency N, averaged over the bottom 500 m.

If the RMS topographic height h_{RMS} at radiating scales implied by $P(k, l; x, y)$ is such that the Froude number Fr is greater than some critical value $Fr_c \sim O(1)$, the energy flux is empirically corrected using Eq. (7). The impact of various values of Fr_c will be investigated in §4.4.

3.3.2 The peaks method

This method is applied to the model's Smith and Sandwell (1997, v15.1) bathymetry in *SS:peaks* and to the GEBCO bathymetry in *GEBCO:peaks*. We use physical ideas about flow blocking, as previously discussed in §2.2, to derive an estimate for lee wave generation given a bathymetry, a bottom flow field (U, V) and a buoyancy frequency N from the model. We take this approach rather than applying a statistical topographic representation such as the Garner (2005) scheme to avoid uncertainties from parameter estimation, and to obtain a local representation whereby we can quantify the energy flux and properties of individual topographic features.

The method is described in full in Appendix C, and is summarised here. First, a peak finding algorithm is used on the relevant bathymetric product to identify locations that have local maxima in the direction of the local flow, defined by the bottom 500 m averaged velocity from the model. Then, a 1D Gaussian is fitted to that peak in the direction of the local flow. The effect of flow blocking is then introduced by modifying the Gaussian to a 'cap' of height $Fr_C U/N$ if the uncorrected height is such that $Fr > Fr_C$. The critical Froude number $Fr_c \sim O(1)$ is not exactly known, and may depend on topographic factors such as the aspect ratio of the topography (e.g. Eckermann et al., 2010), or flow factors such as rotation (Perfect et al., 2020). We will vary Fr_c over values beteen 0.1 and 1 in §4.4.

Figure 1c shows a simplified schematic of the *peaks* method. 1D Gaussian curves (shown in grey) are fitted to the peaks of a section of the bathymetry used in the model, and then capped with an effective height of 100 m (shown in red, corresponding to $U = 0.1\text{m s}^{-1}$, $V = 0$, $N = 0.001\ \text{s}^{-1}$, $Fr_C = 1$). In practise, the orientation of the 1D cap varies with the background flow direction, and the effective height varies with the critical Froude number and the local background stratification and flow speed. In contrast, the full bathymetry with non-propagating scales removed (corresponding to $U = 0.1\ \text{m s}^{-1}$, $V = 0$, $N = 0.001\ \text{s}^{-1}$, $f = 1.2 \times 10^{-4}\ \text{s}^{-1}$) is shown in blue. The difference between the *spectral* and *peaks* methods is illustrated by these differing representations (blue and red, respectively) of the full topography.

Once the blocked 1D Gaussian caps have been found in the whole domain, energy flux can then be inferred. A full explanation of this calculation is given in Appendix C, but we note that assumptions that must be made to infer a 2D flux from 1D topographic profiles do introduce a source of uncertainty into this parameterisation, and the method is only exact for a small amplitude, isotropic Gaussian topography. Complex topography is such that no perfect method exists for determining the 'actual' effective topography (R. B. Smith & Kruse, 2018). Nevertheless, this method produces an estimate of energy flux from actual topographic features, and also allows us to more precisely investigate the height, width, and nonlinearity of the generating topography in a more local way than *spectral* approaches.

3.3.3 The G2010 abyssal hill spectrum

Here, we use the Goff and Jordan (1988) abyssal hill topography (Eq. (6)), with parameters estimated by Goff (2010, 2020); Scott et al. (2011). We use Goff (2010) parameters for k_n, k_s, ν, an updated dataset of $\overline{h^2}$ from Goff (2020), and estimates of θ_s calculated in Scott et al. (2011). These parameters are gridded at 1/15 degree resolution. Where there are missing data (near land, for example), the grid cell is filled with the value of its nearest neighbour, although this does introduce uncertainty.

These parameters are interpolated onto our 1/100° model grid, then the energy flux is found from Eq. (3) using the model bottom velocity and stratification. As in the *spectral* methods, when the RMS height of topography in the radiating range is such that $Fr > Fr_c$, the correction (7) is applied.

3.4 A note on the topographic Froude number

In each parameterisation, the topographic Froude number, $Fr = NH/U$, plays an important role in determining the nonlinearity of the flow and possible necessary corrections due to finite amplitude topography. In the 2D, non-rotating, and hydrostatic limit, Fr is proportional to the ratio of the lee wave vertical wavelength to the topographic height, or equivalently to the ratio of the amplitude of the lee wave horizontal velocity perturbation to the background horizontal velocity (and thus a measure of linearity). This parameter is also sometimes termed the 'steepness parameter', the 'inverse Froude number', the 'Long number', or the 'lee wave Froude number', see F. T. Mayer and Fringer (2017) for discussion.

The bottom background flow speed $U(= |\mathbf{U}|)$ and buoyancy frequency N are defined similarly in each parameterisation, via a 500 m bottom average. However, the characteristic height H is necessarily defined differently in each, since the topographic representations are different. For the *spectral* calculations (*SS:spectral, GEBCO:spectral* and *G2010*), we define the characteristic height as the RMS height, whether that is of the 'full', 'truncated' or 'corrected' bathymetry (see figure 6). This is consistent with previous literature (Nikurashin & Ferrari, 2011; Scott et al., 2011; Nikurashin et al., 2014), and allows our Froude number to directly compare with the critical Froude number of $Fr_C = 0.4$ found by Nikurashin et al. (2014) for energy flux saturation at 2D topography. However, when considering isolated obstacles, the characteristic height is usually defined as the peak height (e.g. Miles & Huppert, 1969; Klymak & Legg, 2010; Eckermann et al., 2010; Perfect et al., 2020). This can lead to some confusion, especially when a critical Froude number is involved. To illustrate this, consider 4 idealised topographies, each with trough to crest heights of h_0:

$$h_1(x,y) = \frac{h_0}{2}\cos kx, \qquad h_2 = \frac{h_0}{2}\cos kx \cos ly \tag{8}$$

$$h_3(x,y) = h_0 e^{-x^2/L^2}, \qquad h_4 = h_0 e^{-(x^2+y^2)/L^2}. \tag{9}$$

Each topography contains peaks of height h_0, yet the corresponding Froude numbers (defined as a RMS for h_1, h_2 and as the peak height for h_3, h_4) are $h_0/2\sqrt{2}$, $h_0/4$, h_0 and h_0 respectively. The different natures of these idealised topographies, and the added complexities of multichromatic topography (discussed by Nikurashin and Ferrari (2010a)) make a consistent characteristic height difficult to define. While the 'cap height' of an isolated obstacle has a physical energetic interpretation (R. B. Smith, 1989), this does not carry over to the RMS definition for complex multichromatic topography, and is one of the reasons that we developed the *peaks* method for a more local representation of topography.

4 Results

4.1 Bottom flow properties

First, we look at the background near-topography flows in the model, which set the conditions under which lee waves are generated. As previously explained, we use daily average fields for 30 days and take an average over the bottom 500 m of the water column. We then smooth the fields slightly with a Gaussian filter with standard deviation of 0.02° to remove any discontinuities caused by abrupt bathymetry.

Figures 4a,b show a daily and 30 day average of the bottom speed $|\mathbf{U}|$. The extreme spatial variability of the flow speed is evident in the 1 day average, and is due to deep reaching eddies with very high bottom velocities of up to 0.5 ms^{-1}. There is some signal of the bathymetry in the 1 day average, especially over the Shackleton Fracture Zone and over the continental shelf, where the depth is less that 1 km - hereafter, we restrict the analysis to regions deeper than 1km to reduce interaction of upper ocean processes and surface reflection with wave generation estimates. In the 30 day mean, the effect of bathymetry on the bottom flow is clearer. Strong bottom currents are steered by the large scale bathymetry through the deep spreading centre of the West Scotia Ridge (running SW-NE, see figure 2c) and its fracture zones (running NW-SE). Despite the flow being deeper at this point, it is faster due to the large scale bathymetry. There are areas of lower bottom speed correlated with shallower bathymetry of the West Scotia Ridge, and above two seamounts near (298.5W, -56.5N), likely due to flow steering around these obstacles forming a stratified Taylor column (Taylor, 1923; Hogg, 1973; Meredith et al., 2015).

Figures 4c,d show the bottom buoyancy frequency N, which is of $O(10^{-3}\mathrm{s}^{-1})$ in most of the domain, but decreases to $2-3\times10^{-4}\mathrm{s}^{-1}$ in deeper parts of the domain, and is considerably higher on the continental shelf (which we exclude from further analyses). The ratio $|\mathbf{U}|/N$ is shown in figures 4e,f, and represents the order of magnitude of the cap height of effective bathymetry seen by the flow, as discussed in §2.2. Due to the high velocities and low stratification in the deep areas of the West Scotia Ridge, this ratio is in places above 1000 m as a 30 day average, implying the potential for extremely large lee wave displacement, if sufficiently high topography exists. Much of the domain has high values of $|\mathbf{U}|/N \sim 300-500$m.

The upper restriction on lee wave wavelength due to rotation is given by $2\pi U/f$ and is shown in figures 4g,h. Due to the locally high velocities, this maximum wavelength can be up to 40 km for the 1 day average, implying that bathymetric scales of up to 40

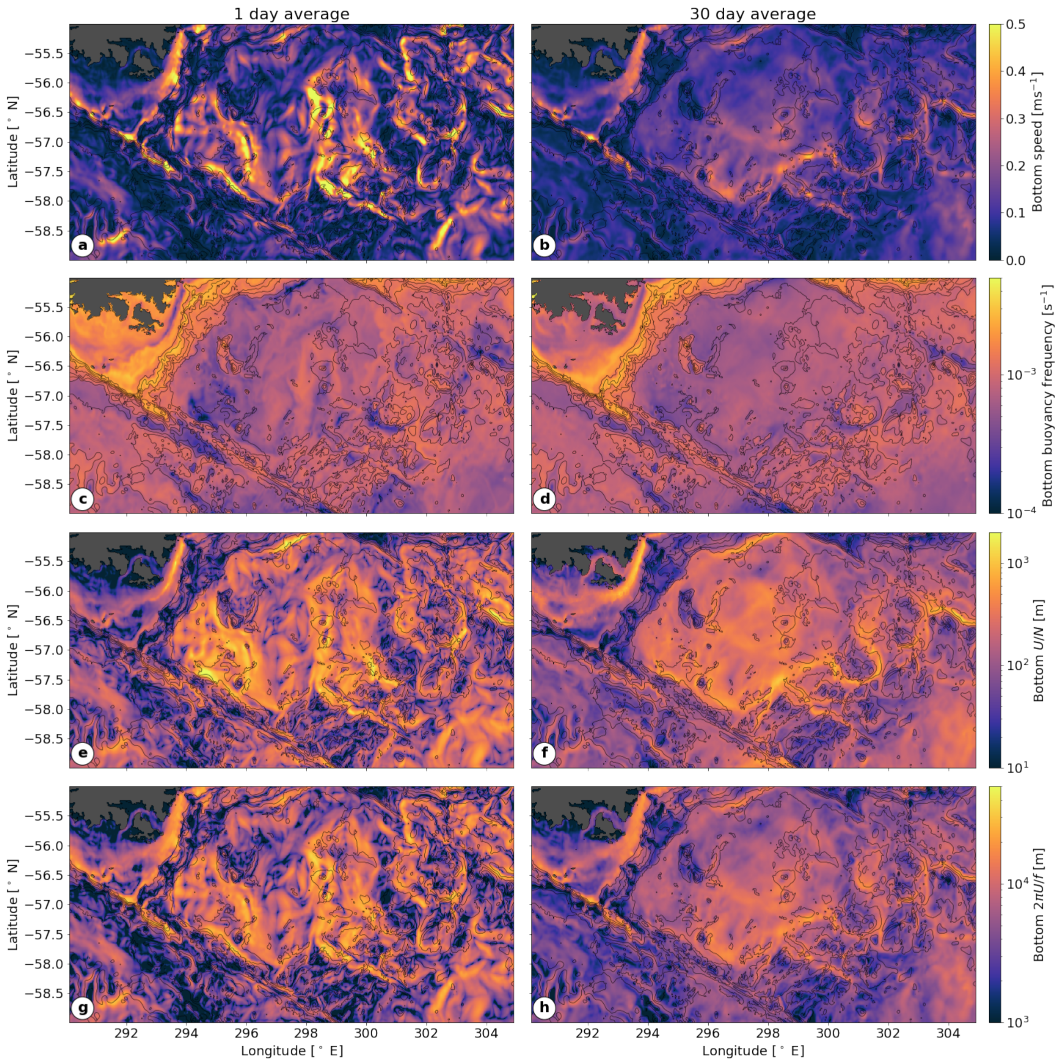

Figure 4. Modelled flows averaged over the bottom 500 m in the Drake Passage, shown as (left) a 1 day average on day 25 and (right) a 30 day average. (a,b): Flow speed $|\mathbf{U}|$, (c,d): buoyancy frequency N, (e,f) $|\mathbf{U}|/N$, representing cap height of topography, and (g,h): $2\pi|\mathbf{U}|/f$, representing the maximum wavelength of radiating lee waves.

km wavelength can generate propagating lee waves in this area. Note that the energy flux (see Eq. (3)) goes to zero as the wavenumber decreases to f/U, thus these very large wavelength lee waves are not expected to contribute significantly to energy flux.

4.2 Resolved wave energy flux

Having described the large scale properties of the bottom flow, we now look into the smaller scale resolved lee wave field. We carried out two filtering methods, as explained in §3.2.

The energy flux calculated from the Lagrangian filtered fields (as explained in §3.2.2) is shown at 500 m above bottom in figure 5a. There are areas of both red (positive energy flux) and blue (negative energy flux), but the positive areas dominate, confirming our expectation that the majority of wave energy in this simulation is generated at and propagating upwards from bathymetry. Areas of negative flux could be due to bottom-generated lee waves reflected from the surface or internal turning levels (Baker & Mashayek, 2021), or to surface generated NIWs propagating downwards (Alford et al., 2016). However, is likely that some of the regions of negative flux are due to horizontal averaging over a non-integer number of wavelengths, non-wavelike processes that survived the *Lagrangian filter*, or wave nonlinearities.

Figure 5b shows the energy flux calculated using the *spatial filter* (explained in §3.2.1) at 500 m above bottom. As for the *Lagrangian filter* in figure 5a, there are areas of both positive and negative energy flux, with positive areas dominating. The spatial variability is similar between the two filters, although the different spatial averaging used in each method is evident.

The fluxes resulting from each method, averaged horizontally in a height above bottom coordinate, are compared in figure 5c. Higher than 500 m above the bottom, both methods show similar results, with similar gradients. The *spatial filter* flux is approximately 15% lower than the *Lagrangian filter* above 500 m above bottom. This suggests that either the *spatial filter* has removed too much of the wave signal (due to the removal of a linear trend, for example, or a too low filter width at 20 km), or the *Lagrangian filter* is picking up energy flux from NIWs that has been filtered out of the *spatial filter* result due to the daily average fields used. In the 500 m nearest to bathymetry, the results diverge from each other and from the expected increase towards bathymetry. This is unsurprising, given the multitude of nonlinear processes (including lee waves) occurring near the bottom. The spatially filtered energy flux goes smoothly to zero, with a maximum at 270 m above bottom. This is due to the reduced effective width of the horizontal sections along which the wave correlations are averaged as topography is approached - part of the section will be below topography and thus excluded from the calculation. The behaviour of the *Lagrangian filtered* energy flux is more erratic - it oscillates in height above bottom, becoming negative near the bottom. We therefore cannot trust either method below 500 m above the bottom. How then, to predict the bottom generated lee wave flux? A major uncertainty in lee wave modelling is the way in which wave energy is deposited by breaking waves above topography. It is also not clear that the model parameterises this decay in a physical way due to the lack of resolution of the wave breaking processes.

Idealised simulations performed by Nikurashin and Ferrari (2010a) of abyssal hill bathymetry representative of the Drake Passage with a topographic Froude number $\geq$ 0.5 found that 50% of wave energy dissipated in the bottom 1km (and 10% with $Fr =$ 0.2). The black and grey vertical lines marked on figure 5c show twice the 1km above bottom values of energy flux from the *spatial* and *Lagrangian filter* respectively. This estimate of wave dissipation with height above bottom (as performed with vertically uniform background fields) does not take into account potential wave-mean interactions which can act to decrease or increase the wave energy flux as the wave propagate through a vertically sheared background flow (Kunze & Lien, 2019; Baker & Mashayek, 2021). Parameterisations for global models using generation estimates of lee wave flux must also empirically determine how the lee wave energy decays with height above bottom - this has been done by assuming exponential decay of energy flux with an e-folding depth of 300 m - 900 m (Nikurashin & Ferrari, 2013; Melet et al., 2014). We therefore fitted exponential curves to the energy flux profiles in figure 5c to extrapolate the more reliable mid-depth energy fluxes to the bottom topography. It is not clear whether these curves should in fact be exponential; depth uniform values of turbulent viscosity and diffusivity (representing wave breaking) in the linear theory imply exponential decay of wave fields with height above bottom (Baker & Mashayek, 2021). It's likely here that an effective turbulent diffusivity would be bottom enhanced, implying a greater-than-exponential decay with height above bottom. This gives a large uncertainty in our bottom estimates of lee wave generation.

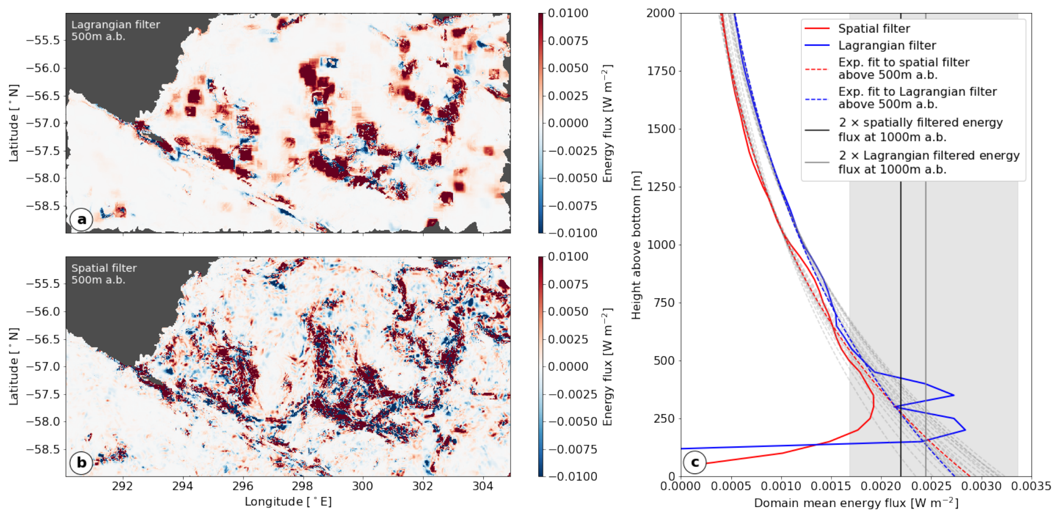

Figure 5. Modelled energy flux using the (a) *Lagrangian filter* and (b) *spatial filter*, at 500 m above bottom, on day 25. The grey areas show either areas with depth less than 1000 m (in the north-west of the domain), or, in (a), the areas at which the *Lagrangian filtered* field isn't available due to tracked water parcels travelling out of the domain. (c) Modelled energy flux on day 25, averaged horizontally in a height above bottom (a.b.) vertical coordinate for the *spatial filter* (red) and the *Lagrangian filter* (blue). Solid lines show the calculated fluxes, grey dashed lines show exponential fits to the calculated fluxes from various heights above bottom ranging from 150 m to 750 m to the surface. Red and blue dashed lines show exponential fits from 500 m above bottom upwards for the *spatial filter* and *Lagrangian filter* respectively. The grey shading shows the region between the value and twice the value of flux at 500 m above bottom from the *spatial filter*.

We fitted exponential curves using least squares regression to the energy flux profiles in figure 5c from various heights above bottom upwards, ranging from 150 m to 750 m (shown in grey dashed); the fits from 500 m above bottom upwards are shown in red dashed for the *spatial filter* and blue dashed for the *Lagrangian filter*. Also plotted is a grey shaded region from the *spatial filter* flux at 500 m above bottom, and twice this value. This region encompasses all of the grey dashed exponential fits, and we use this as a likely conservative bounding region for bottom energy flux. We show this shaded region in later comparisons of resolved energy flux to parameterisations, e.g. figure 9a,b.

For the *spatial filter* method, the wave perturbations need not first be found for the whole 3D field, and can be found directly on a height above bottom surface. This makes the calculation less computationally expensive than the *Lagrangian filter*. This method is also less restricted by available output data, since the *spatial filter* uses daily averaged fields (implicitly low pass filtering in time), whereas the *Lagrangian filter* needs hourly resolution data. Therefore for our calculations hereafter (including 30 day averages), we used the *spatial filter* method at 500 m above bottom, and show the shaded range of likely extrapolated bottom values as in figure 5c. We consider the *Lagrangian filter* to be superior for isolating internal waves, although it can also include the signal of NIWs. The *spatial filter* helps to avoid this, but may remove too much of the lee wave signal.

4.3 Parameterisations: Comparison of topographic representation

The parameterisations use the same bottom flows, but differ in their representation of bathymetry. As discussed in §3.4, the characteristic topographic heights in each method are not directly comparable - in the *peaks* method the characteristic heights are individual peak heights, whereas in the *spectral* method the characteristic heights are RMS heights defined over some local region. Figure 6 demonstrates the differences in these characterisations in terms of topographic heights, and figure 7 for the corresponding Froude numbers.

The top row of figure 6 shows the peak heights from the *SS:peaks* method, each plotted over a 20 km section centred on the peak in the flow direction. Figure 6a shows the full peak heights, which are clearly elevated near the large scale bathymetry of the Shackleton Fracture Zone and West Scotia Ridge (see figure 2c), and exceed 700 m in places. The corresponding Froude numbers (figure 7a) are extremely large (above 10), indicating considerable flow blocking by the large scale topography. When blocking by the modelled flow is taken into account, (figure 6b, $Fr_C = 1$) the distribution of high peaks becomes more uniform, with many peaks exceeding 150 m in height. Figure 7b indicates that in the regions of rough topography, many of the blocked Froude numbers are between 0.8 and 1, indicating significant flow nonlinearity, with potential for hydraulic jumps and wave breaking above topography. When these peak profiles are truncated to wave radiating scales, the effective heights (or equivalently the maximum lee wave displacements) decrease, but still exceed 150 m in places, indicating that large wave displacements can be expected. The corresponding Froude numbers (now indicating the likely nonlinearity of the waves) remain high (above 0.5) over the regions of rough topography, thus we expect a highly nonlinear wave field.

The middle row of figure 6 shows the *SS:spectral* method RMS heights, and the nonlocality of the characteristic heights is clear when compared to the *SS:peaks* in the top row. The full RMS topographic height (figure 6d) at scales less than 50 km shows clearly the large scale bathymetry of the Shackleton Fracture Zone and West Scotia Ridge, with large RMS heights of 500-700 m. However, when the spectrum at each location is truncated to radiating scales using the local flow, the RMS height falls considerably. The signature of the bottom flow speed (see figure 4b) is clearly visible - higher bottom flow speeds allow a larger maximum radiating wavelength of $2\pi|\mathbf{U}|/f$, and thus larger topographic heights. The corresponding Froude numbers (figure 7e) are significantly reduced, and are almost everywhere below 0.3, although there are higher Froude numbers over the rougher topography. The nonlinear correction at $Fr_C = 0.4$ (the relevant critical Froude number found by Nikurashin et al. (2014) for 2D spectral topography, applied similarly to the energy flux correction in Eq. (7)), then, does not have a large effect on the characteristic height (figure 6f) or Froude number (figure 7f) aside from near the continental shelf, suggesting that flow blocking is negligible.

The *G2010* method characteristic (RMS) heights are shown in the bottom row of figure 6. There is not good agreement between this abyssal hill estimate (figure 6g) and the *SS:spectral* (figure 6d) at scales less than 50 km, because the former intentionally does not include large scale bathymetry. However, when truncated to radiating scales, there is good spatial agreement between the RMS heights calculated spectrally from the bathymetry used in the model (figure 6e) and the G2010 abyssal hill spectrum (figure 6f), showing the skill of the G2010 abyssal hill estimates. The domain averaged RMS height and Froude number at radiating scales (uncorrected) are lower in *SS:spectral* (RMS $h = 16$ m, $Fr = 0.08$), compared to RMS $h = 21$ m, $Fr = 0.14$ in *G2010*.

The *SS:spectral* method (with saturation of energy flux above Fr_C) aims to represent the topography at lee wave radiating scales only, whereas through the *SS:peaks* method, we aim to represent the effective topography 'seen' by a flow as it passes, whether that is at radiating lee wave scales, or at larger scales whereby the disturbance to the

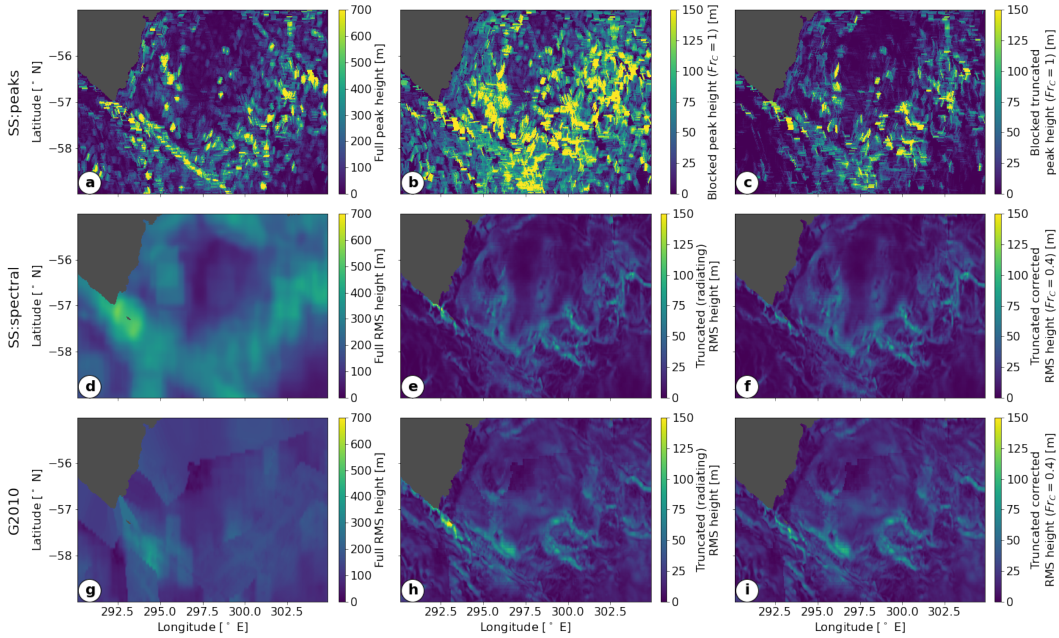

Figure 6. Various representations of 30 day average topographic heights in our parameterisations. Top row: *SS:peaks*. (a) Full peak heights from fitted Gaussians (c.f. grey curves in figure 1c), (b) blocked peak heights at $Fr_C = 1$ (c.f. red curves in figure 1c), and (c) blocked truncated peak height, calculated as the range of heights in the blocked Gaussian profile when non-radiating scales are removed. Middle row: *SS:spectral*. (d) RMS height including all topographic wavelengths < 50 km, (e) RMS height including only radiating topographic wavelengths, (f) RMS height including only radiating topographic wavelengths, corrected for $Fr_C = 0.4$ similarly to Eq. (7). Bottom row: as for middle row, with *G2010* representation of abyssal hill topography.

flow is non-propagating. To validate the parameterisations against the numerical simulation, we later (see §4.4) compare energy flux from the parameterised ans simulated wave field. However, calculation of resolved wave energy flux in the model is difficult, wave resolution likely depends on horizontal and vertical model resolution, and a large uncertainty is introduced by the need to estimate the rate of decay of the wave field with height above bottom. A more readily available variable for comparing the effective topographies is the RMS bottom vertical velocity.

In the both the simulation and parameterisations, a no-penetration boundary condition holds at the topography

$$w = \mathbf{u}_H \cdot \nabla_H h(x, y) \tag{10}$$

$$\simeq \mathbf{u}_H \cdot \nabla_H h_{\text{eff}}(x, y) \tag{11}$$

where w is the total vertical velocity, $\mathbf{u}_H$ is the total horizontal flow, ∇_H is the horizontal gradient, $h(x, y)$ is the full topography, and $h_{\text{eff}}(x, y)$ is the effective topography seen by the flow. The second equality (11) arises from observing that when the flow is blocked or split, there is very little vertical component to the flow since $\mathbf{U}_H$ is perpendicular to $\nabla_H h$. The bottom vertical velocity can therefore be seen as a proxy for the effective topography seen by the flow.

In the linear parameterisations, this boundary condition is also free slip and linearised so that it acts at $z = 0$; this is equivalent to neglecting quadratic wave pertur-

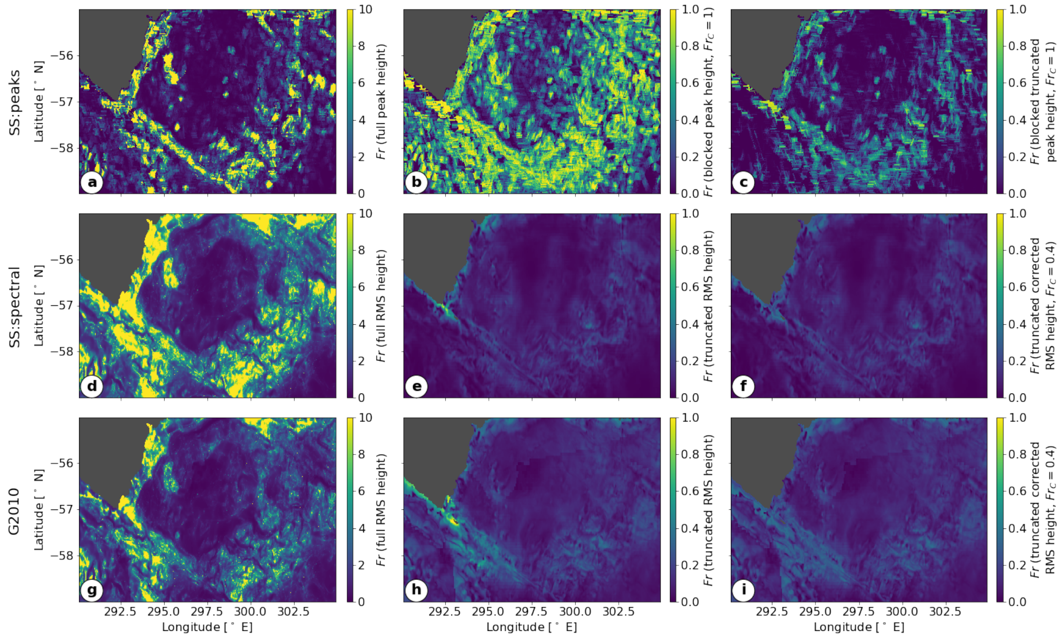

Figure 7. 30 day average topographic Froude number, calculated as $NH/|\mathbf{U}|$, where characteristic height H for each panel is as in figure 6.

bation terms in the derivation of the linear theory. Assuming that this is valid, $\overline{w^2}$ can be found in a similar way to the energy flux (c.f. Eq. (3)). Note that the partial isotropy assumption and the correction for 2D topography used in the *peaks* method energy flux (Eq. (C11)) is not necessary here. In the simulations, there is a no-slip bottom boundary condition and a quadratic drag in addition to Eq. (10). Assuming that this friction acts in a thin bottom boundary layer and thus does not greatly affect the bottom 500 m averaged velocities, the bottom RMS w can be calculated from the simulated vertical velocity field. In both cases, we can calculate both the total vertical velocity (as determined by the boundary condition Eq. (10)) and the propagating part associated with lee waves. In the case of the simulations, we use the *Lagrangian filtered* vertical velocity for this (as shown in figure 3d) on day 25.

Figure 8 shows the 30 day average total (radiating and non-radiating) RMS bottom vertical velocity calculated from the model (figure 8a), the *peaks* method (figure 8b) and the *spectral* method (figure 8c). Both the *spectral* and *peaks* results are shown with $Fr_C = 1$, with the *spectral* method calculation corrected in a similar way to Eq. (7). Spatially, they show the same patterns - bottom vertical velocity is enhanced at rough topography and where flow speeds are high. However, the *spectral* method predicts higher vertical velocities throughout - this is expected, as the saturation of the *spectral* method is only empirically verified for lee wave generating scales. The *peaks* method recreates the vertical velocity field of the simulation well, including many of the small scale features that the *spectral* method misses, since it is inherently non-local.

Figure 8d shows the domain average RMS w against critical Froude number for the simulation and parameterisations. As seen from the spatial maps, the propagating *SS:spectral* estimate is significantly higher than the *SS:peaks* estimate - over 3 times larger at small Fr_C and nearly twice as large at large Fr_C. The *SS:spectral* estimate does not intercept the simulation estimate at any Fr_C, whereas the *SS:peaks* estimate predicts the simulated propagating RMS w correctly when $Fr_C = 0.8$, and total RMS w at $Fr_C = 1$, both realistic values (Perfect et al., 2020). The parameterised and simulated RMS w es-

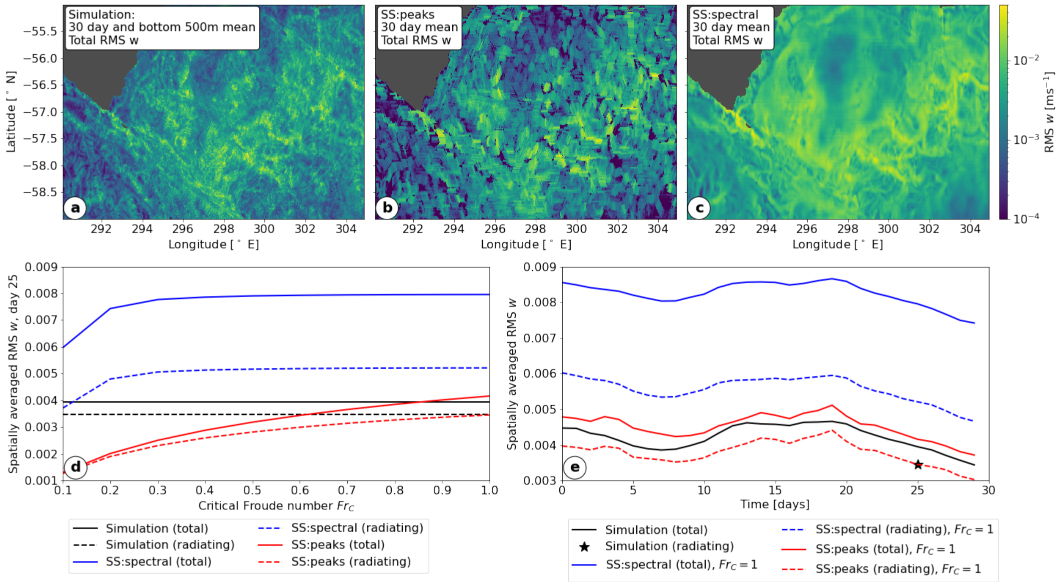

Figure 8. Comparison of total RMS vertical velocity between parameterisations. (a) Bottom 500 m and 30 day averaged model vertical velocity (b) *SS:peaks* bottom RMS vertical velocity, $Fr_C = 1$, (c) *SS:spectral* bottom RMS vertical velocity, $Fr_C = 1$. (d) Domain averaged bottom RMS vertical velocity (propagating and total) against Fr_C, and (e) Time evolution of domain averaged bottom RMS vertical velocity. The propagating component of the simulated vertical velocity is shown by a star for day 25 only (where we have *Lagrangian filtered* output data).

timates are plotted against time in figure 8e for $Fr_C = 1$ in figure 8d, although note that the results for the *spectral* method are insensitive to $Fr_C \gtrsim 0.3$. The *peaks* method captures the temporal evolution of the model well, and although the *spectral* method also captures some of the temporal evolution, it is consistently too high. This suggests that a) the *peaks* representation does appear to adequately characterise the effective topography on radiating and non-radiating scales, and b) the *spectral* method overestimates the topographic variation, especially on non-radiating scales.

4.4 Parameterisations: Comparison of energy flux

We next compare parameterised and resolved energy fluxes. Figure 9a shows each of these domain and 30 day averaged estimates against the critical Froude number used in the parameterisations. Our estimate of bounds for the resolved energy flux at topography in the simulations is shown by the grey shaded region, and does not vary with Fr_C, which can be seen as a tunable parameter in the parameterisations. The hydrostatic *SS:spectral* and *SS:peaks* methods are shown in solid blue and red respectively, and these can be directly compared to the (hydrostatic) model energy flux. The *peaks* representation increases across all Fr_C, suggesting that the topography represented is significantly blocked, and the resulting wave field likely to be nonlinear. The *peaks* energy flux agrees with the resolved energy flux at $Fr_C \sim 0.3{-}0.4$, in contrast to the agreement in figure 8 at $Fr_C \sim 0.8{-}1$ for RMS vertical velocity, suggesting that the *peaks* parameterisation has inconsistencies. We hypothesise several potential reasons for this. Firstly, it is likely that the wave energy flux in the model is not fully resolved or filtered, and therefore underestimated. Secondly, it is unclear whether the exponential extrapolation of the wave energy flux in figure 5 is appropriate - parameterised vertical turbulent diffusivity and viscosity through the KPP scheme in the model are enhanced in the bottom 500 m or so, and

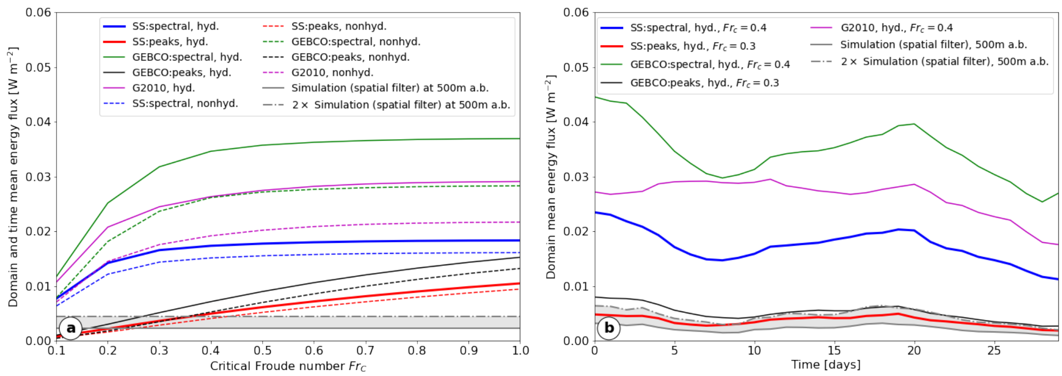

Figure 9. Domain mean energy flux from parameterisations and simulations against (a) critical Froude number Fr_C (30 day mean) and (b) time (at specified Fr_C). The shaded grey region shows the likely range for resolved energy flux at topography in the simulations (see figure 5c). Solid and dashed lines represent hydrostatic (hyd.) and nonhydrostatic (nonhyd.) calculations repectively.

may significantly dissipate the generated lee waves, a mechanism discussed by (Shakespeare & Hogg, 2017). Finally, the estimation of energy flux in the *peaks* method requires a partial isotropy assumption (see Appendix C, Eq. (C11)), which may cause an underestimation of energy flux. This assumption is not necessary for the calculation of RMS vertical velocity.

The *SS:spectral* method predicts higher energy flux than the *SS:peaks* method, especially at lower Fr_C (figure 9a). The *SS:spectral* energy flux stops increasing at $Fr_C \sim 0.4$, suggesting (as in figures 7e,f) that the resulting flow is fairly linear, and does not need a saturation correction - contrary to the *peaks* representation. Using the GEBCO bathymetry with both the *spectral* and *peaks* methods significantly increases the energy flux - more so with the *spectral* method, where energy flux for $Fr_C \gtrsim 0.4$ is doubled. This suggests that the updated GEBCO bathymetry has far superior resolution of the lee wave generating topography than the older version of bathymetry used in the model. We also plot the energy flux calculated with the G2010 abyssal hill spectrum - this follows a similar trend to the other *spectral* methods, and energy flux lies between the *SS:spectral* and *GEBCO:spectral* estimates.

In order to directly compare the energy flux estimates from resolved multibeam bathymetry with abyssal hill estimates, we also show the energy fluxes plotted in figure 9a restricted to the areas of the domain where the GEBCO dataset contains multibeam bathymetry - this area is shown in figure 10 and covers 70% of the domain deeper than 1000 m. In the case of the *GEBCO:peaks* estimate (which uses the local topography at each location), this does effectively restrict to lee wave flux generated by resolved features, whereas the *spectral* estimates use the surrounding 100 km by 100 km area of topography to calculate the 'local' spectrum, so this separation is not as clean. Similarly to figure 9a, the *G2010* estimate lies between the *GEBCO:peaks* and *GEBCO:spectral* estimates. The hydrostatic *GEBCO:spectral* estimate at $Fr_C = 1$ is 38% greater than the corresponding *G2010* estimate, suggesting that larger non-abyssal hill scales may be important for lee wave energy flux, consistent with observational evidence in the Drake Passage (St. Laurent et al., 2012; Cusack et al., 2017). It is important to note, however, that comparison of the *peaks* and *spectral* methods in the current study has shown that a spectral representation of a realistic topography that is truncated above some topographic wavelength, as in *GEBCO:spectral*, may not be appropriate.

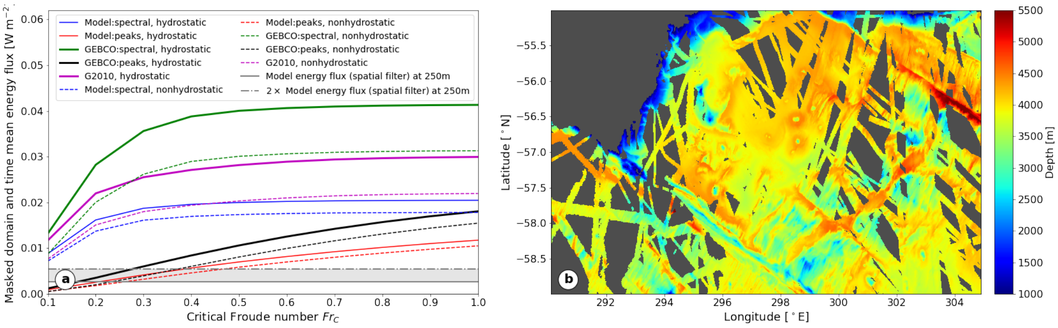

Figure 10. (a) As in figure 9a, but spatially averaged over the unmasked domain shown in (b), which shows where the GEBCO dataset contains multibeam bathymetry.

For best comparison with the hydrostatic simulations, we have so far used the hydrostatic approximation in our parameterisations. The nonhydrostatic calculations of parameterised energy flux are shown as dashed lines in figures 9a, 10a . These show that nonhydrostaticity is important in this region, significantly reducing lee wave energy flux. This effect is the most significant in the topographic representations that contain the smaller scales: *G2010* (25% reduction), *GEBCO:spectral* (23% reduction), and *GEBCO:peaks* (13% reduction), each stated for the whole spatial domain and at $Fr_C = 1$.

The *GEBCO:peaks*, *GEBCO:spectral*, and *G2010* estimates in figure 10a can also be compared to previous estimates of energy flux estimates in the Drake Passage. The global (nonhydrostatic) estimate of Nikurashin and Ferrari (2011) found an energy flux of 0.037 kg m s^{-1} spatially averaged over our Drake Passage domain, which is consistent with our *spectral* estimates in figure 10. Yang et al. (2018) considered various abyssal hill estimates, finding a Drake Passage-averaged energy flux of 0.018 kg m s^{-1} (with Goff (2010) topographic parameters), 0.012 kg m s^{-1} (with Goff and Arbic (2010) topographic parameters) and 0.009 kg m s^{-1} (with Nikurashin and Ferrari (2011) topographic parameters), each using energy saturation with a critical Froude number of 0.4. These estimates are lower than estimates by Nikurashin and Ferrari (2011); Scott et al. (2011), which Yang et al. (2018) attribute to differences in the modelled near bottom velocity and stratification, but these estimates are also of the same order of magnitude to ours.

The temporal evolution of the spatially averaged parameterised and modelled energy flux is shown in figure 9b. The simulated energy flux shows a similar time evolution to each parameterisation, especially for the *peaks* methods. The spatial patterns of energy flux for each parameterisation are shown in figure 11, showing that they largely recreate the patterns of the simulated energy flux, although each parameterisation has strictly positive energy flux by construction. The *spectral* estimates, shown for $Fr_C =$ 0.4 to be consistent with the results of Nikurashin et al. (2014), are much higher than the *peaks* estimates, which show fairly good correspondence with the simulated energy flux (note that these are shown for $Fr_C = 0.3$ for best match to the simulations, as in figure 9a). The spatial patterns of energy flux largely coincide with the areas of high bottom velocity shown in figure 4b.

Finally, we compare the spectral characteristics of each parameterisation; we were unable to calculate a good estimate of the spectrum of the resolved energy flux from the simulations near topography, since the flow field has missing data where topography intersects any horizontal plane. Figure 12 shows the topographic and energy spectra for each of the *spectral* methods. It is clear that the *GEBCO:spectral* topographic and energy spectra have power at smaller scales that are absent in *SS:spectral* due to the limited spatial resolution of the bathymetry used in the model. Power in the *GEBCO:spectral*

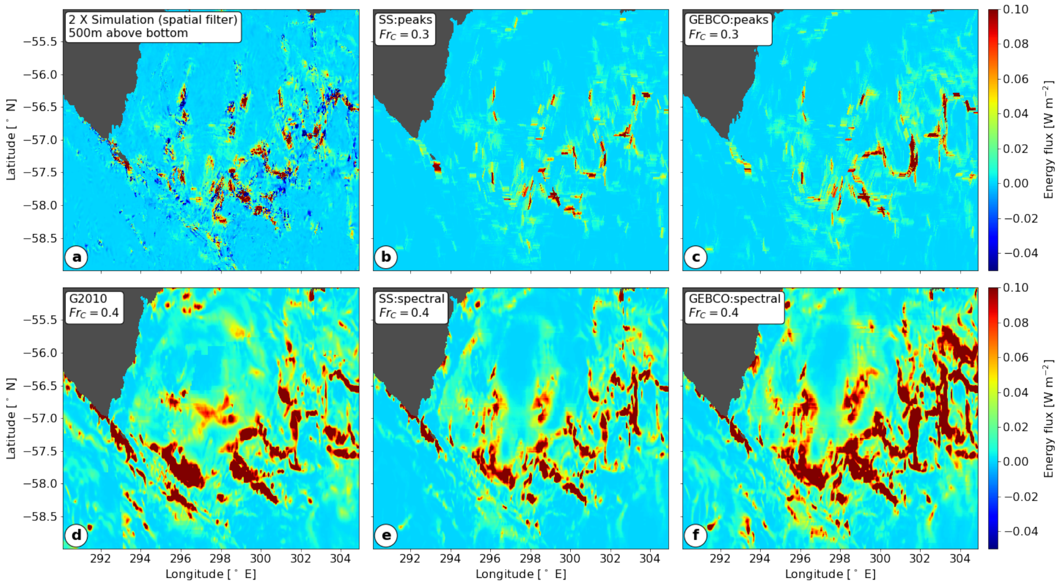

Figure 11. 30 day average energy flux from (a) the modelled wave field; twice the flux at 500 m above bottom is shown, calculated using the *spatial filter* (c.f. figure 5c), and (b)-(f) each parameterisation.

topographic spectrum is also greater at large topographic scales, and there is some unphysical spurious signal at smaller scales (figure 12b). The *G2010* topographic spectrum (figure 12c) has similar order of magnitude, but the spectrum has a more defined anisotropy. This isotropy is also visible in *GEBCO:spectral* (figure 12b), but not the model bathymetry spectrum (figure 12a), suggesting that the anisotropy is associated with abyssal hills that are preferentially orientated relative to large scale topographic features (Goff & Jordan, 1988), and not resolved in the bathymetry used in the model. The energy spectra follow a largely similar pattern to the topographic spectra, with the exception of a reduction of energy towards zero at large topographic wavelengths due to rotation.

In order to show the amplitudes of the energy spectra more clearly, we plot a 1D version of the 2D spectra shown in 12 in figure 13a. Each spectrum has a peak at a modal wavelength of ~ 10 km, which is large compared to the modal wavelength of 5 km found by Scott et al. (2011) for lee wave energy flux in Southern Hemisphere, and reflects the especially high bottom velocities in the Drake Passage. Both hydrostatic and nonhydrostatic energy spectra are shown, and, consistent with figure 9, the nonhydrostatic calculation is smaller at every wavenumber, but more so for larger wavenumbers (as expected from Eq. (3)). The GEBCO dataset generates the most energy flux at wavelengths larger than $\sim$ 3 km ($|\mathbf{k}| \lesssim 0.002$), below which the G2010 abyssal hill estimate dominates. *SS:spectral* has slightly larger energy flux than *G2010* at wavelengths above ~ 8 km ($|\mathbf{k}| \lesssim 0.0008$), but significantly less at smaller scales.

Figure 13b shows the cumulative distribution function (CDF) of each of the spectra in figure 13a. Vertical lines show the x-intercepts of the 50% and and 90% levels, thus we see that using the model bathymetry, 90% of the energy flux occurs at wavelengths larger than 4 km (nonhydrostatic), whereas 90% of the energy flux from the G2010 bathymetry occurs at wavelengths larger than 2.5 km. For reference, Scott et al. (2011) found that globally 90% of lee wave generation is between horizontal wavelengths of ~ 1.1 km and ~ 16 km. This calculation also allows inferences of the necessary model horizontal grid resolution to resolve a given proportion of lee wave energy. With reference to our hydro-

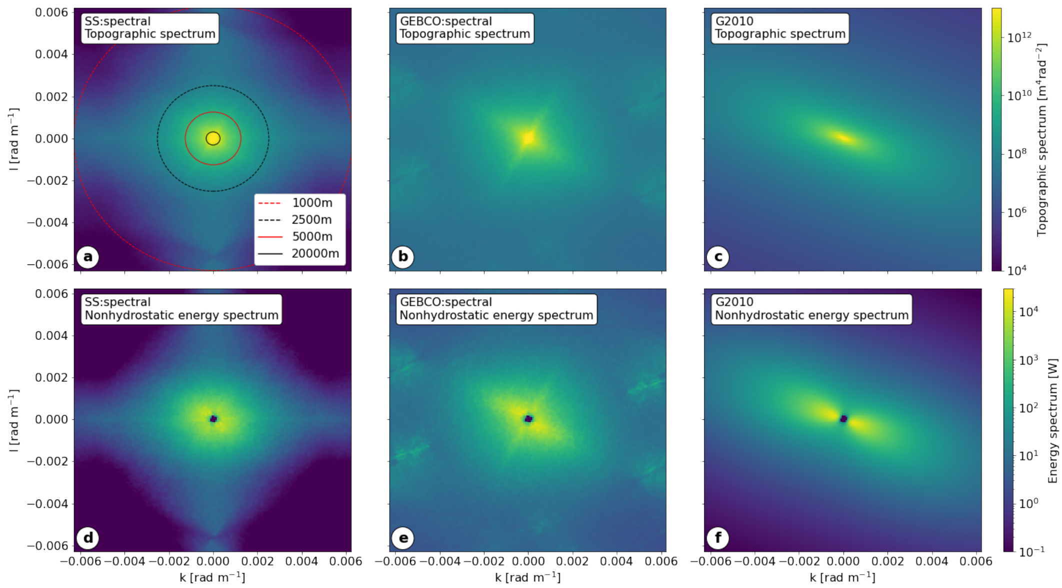

Figure 12. Top row: topographic spectra and bottom row: energy flux spectra. All spectra are averaged over the domain and 30 days. Topographic representation used is indicated in the labels.

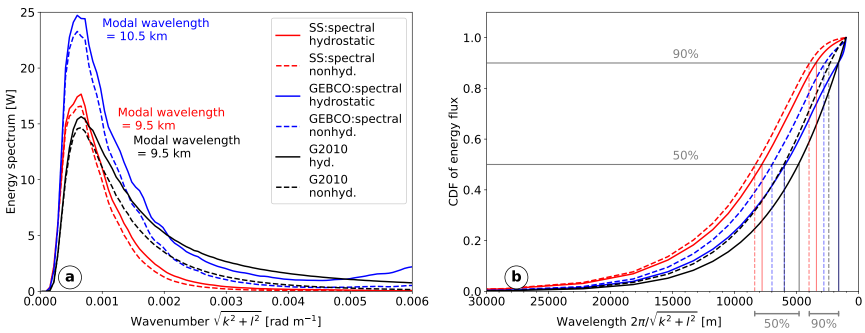

Figure 13. (a) 1D Energy flux spectra and b) CDF of energy flux with wavelength for each spectral topographic representation. Vertical lines in (b) allow the 50% and 90% levels to be read off from the wavelength (x) axis. Solid and dashed lines represent hydrostatic (hyd.) and nonhydrostatic (nonhyd.) calculations repectively.

static simulation with its existing bathymetry, it suggests that to allow 90% of lee wave energy to be resolved, the model must be able to resolve wavelengths of 3.5km. Our 0.01° horizontal resolution gives a N-S resolution of 1112m and a maximum W-E resolution of 638 m. In an atmospheric study of mountain waves, Vosper et al. (2020) found that wave drag decreased rapidly once the wavelengths were smaller than 5-8 times the grid scale. This suggests that we fully resolve wavelengths greater than 5560-8900 m (N-S) and 2860-5100 m (E-W), which would imply from figure 13 that 5-60% of the expected energy flux in our model could be unresolved - although it is likely that some percentage of this missing flux is present in the simulations. With a more resolved bathymetry such as GEBCO, or an abyssal hill bathymetry such as G2010, the necessary horizontal resolution to resolve 90% of the flux in a nonhydrostatic model would be $\sim 300 - 500$ m.

The vertical resolution of the numerical model also has a significant effect on lee wave generation; a previous version of our simulation with 100 vertical levels rather than the current 225 levels, and 100 m vertical grid spacing below 2500 m, was unable to sufficiently resolve the topography for lee wave generation (Mashayek, Ferrari, et al., 2017). Horizontal and vertical resolution of ocean and climate models will soon increase into the 'grey zone' (Vosper et al., 2016), in which wave processes are neither fully resolved nor fully sub-grid-scale. Careful consideration of the overlap of parameterisations with resolved processes will therefore become increasingly important. For ocean models that attempt to resolve bottom generated internal waves and other processes, it may be necessary to increase vertical resolution of the model grid near the sea-floor in a similar way to the typical increase of vertical resolution near the surface.

5 Summary

Parameterisations of mixing and dissipation due to bottom generated lee waves in ocean require knowledge of the sea-floor topography. Representing this topography in the global parameterisations is a challenging task because oceanic bathymetry is not sufficiently resolved, so statistical estimates of abyssal hills informed by topographic data are used to represent topography on lee wave generating scales (Goff & Jordan, 1988). Furthermore, linear theory for lee wave generation does not apply when the flow is blocked or split at tall topography, so empirical corrections must be made to lee wave energy flux estimates. Here, we developed several different representations of a realistic region of topography, and compared the impact on the resulting lee wave energy flux. We asked the question: if we know some complex, realistic, flow and bathymetry, can we predict the lee wave energy flux, and how does this compare to abyssal hill estimates?

To do this, we used a realistic, wave resolving simulation of the Drake Passage, a region of high lee wave generation. We first calculated the energy flux into lee waves in the simulation, comparing two different wave filtering methods. We then compared this energy flux with that calculated using linear theory and several different representations of topography. In particular, we compared *spectral* methods, whereby the realistic Drake Passage bathymetry was spectrally high pass filtered to only include topographic wavelengths that allowed radiating lee waves before empirical corrections for nonlinearity were applied, with our own *peaks* method. This method represented the realistic topography as an ensemble of Gaussian peaks. Each peak was considered individually, and its height adjusted to account for flow blocking at some critical Froude number, allowing topographic blocking to be represented in a more physical way. In addition to topographic representations that aimed to represent the bathymetry that was used in our simulation, we also compared our results to energy flux implied by the Goff and Jordan (1988) abyssal hill spectrum, which is commonly used in oceanic lee wave parameterisations.

We found that the *spectral* representation of realistic bathymetry may overestimate the energy flux at topography, whereas the *peaks* method was able to recreate the modelled energy flux for sensible values of the critical Froude number. We also compared the inferred RMS vertical velocity from the simulation and parameterisations, as it is a more readily available and direct proxy for the effective topography for lee wave generation. We found that, whereas the *spectral* representation overestimated both the total and the radiating part of the RMS vertical velocity, the *peaks* representation was able to capture the amplitude and horizontal spatial structure of the radiating and total components of the RMS vertical velocity. We concluded that the *spectral* topographic representations may overestimate lee wave generation due to their inability to take into account flow blocking before the truncation to propagating scales, resulting in spurious small scales arising from the spectral truncation of large scale topography. We also found that energy flux calculated spectrally from multibeam areas of resolved bathymetry in the region was 38% higher than that calculated with the abyssal hill estimates. This implies (assuming validity of spectral methods) that the non-abyssal hill topography is important for lee wave generation in the Drake Passage, consistent with observational evidence (St. Laurent et al., 2012; Cusack et al., 2017).

We also found that the *spectral* method may misrepresent the nature of the lee wave field, in particular the nonlinearity and heterogeneity. The *spectral* method, relying on a RMS representation of topographic height, predicts topographic Froude numbers $\leq$ 0.4 almost everywhere in the domain, implying a fairly linear wave field. Linear lee waves generated from a periodic bathymetry are not expected to become unstable and break through shear or convective instability, and have instead been predicted to decay due to interactions with vertical shear from inertial oscillations (Nikurashin & Ferrari, 2010b). However, the *peaks* method predicts that there are many peaks where the Froude number is $\simeq 0.8$, implying nonlinear and isolated lee waves, which can overturn and break above topography in a fashion that is more commonly associated with atmospheric mountain waves. The regime of lee wave generation implied by the *peaks* method would be associated with enhanced drag (Peltier & Clark, 1979; Durran, 1986; Epifanio & Durran, 2001) and vigorous hotspots of lee wave breaking, potentially with high mixing efficiency due to convective overturns (Chalamalla & Sarkar, 2015). The heterogeneity of the bottom velocity field due to eddies and steering from larger scale topography leads to a patchy distribution of lee wave energy, implying that locality in the parameterisations of lee waves is important. Large energy flux from isolated patches of high bottom velocity often propagate to and reflect from the surface in our model, interacting with both the background flow and the reflected waves through constructive and destructive interference (Baker & Mashayek, 2021).

6 Caveats

Our results come with a number of uncertainties and caveats that require further study. Despite containing an energetic lee wave field, our simulations likely do not resolve the entire lee wave spectrum, and sensitivity to vertical and horizontal resolution of such wave resolving models should be investigated further. Another substantial challenge arises from the need to parameterise sub-grid-scale wave breaking in such models, and this introduces further uncertainty in our estimates. We tested two filtering methods to extract the lee wave field from the total flow, but a lack of ground truth in how waves should be separated from the rest of the flow makes this a difficult task. Choices were also required in the development of the *spectral* and *peaks* representations from the realistic bathymetry, and careful sensitivity studies in idealised settings would be necessary before drawing firm conclusions about the efficacy of each.

We have pushed the assumptions of the linear theory, as is typical in oceanic lee wave parameterisations. In particular, assumptions on the uniformity of background flow are likely to be invalid. We have assumed that the background flows are horizontally and vertically uniform on the scales of lee wave generation - this is not the case in this domain, where large vertical wavelengths can be of a similar scale to vertical changes of the background flow. Horizontal variations of the background flow are created by the larger scale topographic features (e.g. figure 4a), and therefore the flow does vary on scales that overlap with the spectrum of lee wave generation. Furthermore, we have assumed that the background flow is steady on the timescale of lee wave generation, and neglected transient wave generation. However, in comparing parameterisations of lee wave energy flux with nonlinear simulations of realistic resolved wave energy flux, this work represents progress towards validating some of these assumptions.

7 Future directions

Our findings imply that spectral topographic representation techniques used to construct current ocean model parameterisations may lead to overestimates of lee wave dissipation and mixing in areas of rough topography, which could have implications for the large scale circulation. We also found that the nonlinearity of the wave field may be underestimated, which could lead to misguided assumptions about the mechanisms and spatial distribution of wave breaking and subsequent mixing and dissipation. Study of regions with different topographic characteristics and with simplifications such as an idealised flow would help to verify the these findings.

Although we have considered only bottom-generated waves generated by a quasi-steady flow throughout, estimates of internal tide generation also depend on an abyssal hill representation of topography. The impact of an 'effective topography' on internal tide energy flux could also be investigated using this framework. Understanding of the impact of other bottom processes, such as arrested Ekman layers, hydraulic jumps, and wake vortices could also benefit from improvements in topographic representation.

Our *peaks* topographic representation suggests the need for real topographic data for calculation of energy flux, which is currently not possible globally due to insufficient multi-beam sea-floor data. However, the Nippon Foundation-GEBCO Seabed 2030 Project (L. Mayer et al., 2018) aims to map 100% of the sea-floor by 2030, so it is likely that in the next decade data coverage will significantly improve. Parameterisations of bottom generated processes such as lee waves will then require techniques such as our *peaks* method to capitalise on this hard-won dataset. Even in coarse resolution models, online parameterisations could take into account this high resolution bathymetry in calculating wave energy flux. It is therefore timely to consider the improvements to parameterisations that may be made with improved resolution of sea-floor topography.

Appendix A The spatial directional filter

We develop a spatial directional filter help us to separate lee waves from other low frequency flow structures with similar spatial scales. We exploit the general characteristic of lee waves that the wave crests are perpendicular to the flow direction (neglecting 3D effects).

To determine a wave correlation term at some location, for example $\overline{uw}$, we first define the background flow at that location as the 20 km low passed flow field (performed using a horizontal 2D uniform filter of width 20 km). We then use this background flow to determine the flow direction, and bin this into 4 categories based on the compass directions: NS (& SN), WE (& EW), NW-SE (& SE-NW) and NE-SW (& SW-NE). We then extract one dimensional 'strikes' of length 20 km in this direction of the high passed wave fields u and w. We remove any linear trend from each, multiply them together, and take an average to give the relevant term (here, $\overline{uw}$) at that location.

Appendix B The *spectral* topographic representation

This method is applied to both the Smith and Sandwell (1997, v15.1) bathymetry used in the model *SS:spectral* and the GEBCO bathymetry *GEBCO:spectral*. We represent bathymetry $h(x, y)$, where x and y are longitude and latitude, by a topographic spectrum $P(k, l; x, y)$ at each model gridpoint.

We are interested in the properties of the bathymetry on the most granular scale possible, in order to understand the impact of the complex bathymetric features in our domain. To do so, we use a sliding window Fourier transform, whereby the signal (here, the bathymetry) is multiplied by a window function that restricts to some smaller spatial domain and brings the signal to zero at the domain edges to avoid spectral sidelobe issues. However, there is an inherent difficulty associated with finding a 'local' spectral representation due to the 'uncertainty principle in signal processing' (analagous to the Heisenburg uncertainty principle in quantum mechanics), or Gabor Limit (Gabor, 1946). There is a limitation in the joint spectral and spatial resolution, which in our case means a trade-off between window size (and hence localisation of signal) and wavenumber resolution. We find that a 2D window size of 100 km $\times$ 100 km (and thus a wavenumber resolution of $2\pi\times10^{-5}$ rad m^{-1}) keeps errors in energy flux calculations due to limited wavenumber resolution below 1%, whilst still allowing some localisation of the topographic spectra.

First, we take the original model topography h (including the sponge layer region to avoid missing data at the edges). We remove a 50 km smoothed bathymetry using a uniform filter from the original, leaving us with a bathymetry $h_{hp}(x, y)$ that still contains all lee wave generating scales. 50 km is chosen as it is the maximum bottom value of $2\pi U/f$ in the domain, hence the maximum possible lee wave generating scale.

At each grid location, we interpolate the high pass lat-lon (x, y) model grid onto a 100 km by 100 km regular grid (X, Y) at 500 m resolution, where the origin $(X, Y) = (0, 0)$ is at (x, y). We then apply a Hann windowing function $\mathcal{F}_H(X, Y)$ to h_{hp}, to give $h_f(X, Y) = h_{hp}(X, Y)\mathcal{F}_H(X, Y)$, where

$$\mathcal{F}_H(X, Y) = \frac{1}{4}(1 + \cos \pi X/L)(1 + \cos \pi Y/L) \tag{B1}$$

where $(X, Y) = (0, 0)$ is the local coordinate of the point at which we wish to find the spectrum, and $L = 50$ km. This filter brings h_f to zero at the edges of the patch, removing sidelobe issues when a Fourier transform is taken. h_f is then renormalised so that $\overline{h_f^2} = \overline{h_{hp}^2}$. $\mathcal{F}_H$ itself has wavelength outside of the propagating wavelengths, so although this filtering does modify the spectrum, it doesn't significantly affect the lee wave generating scales.

The Fourier transform $\hat{h}(k, l)$ of $h_f(X, Y)$ is then found through

$$\hat{h}(k, l) = \int_{-L}^{L} \int_{-L}^{L} h_f(X, Y) e^{-i(kX+lY)}\, dX\, dY \tag{B2}$$

and the topographic power spectrum is given by $P(k, l; x, y) = \frac{1}{4L^2}|\hat{h}(k, l)|^2$.

Appendix C The *peaks* topographic representation

This method is applied to the Smith and Sandwell (1997, v15.1) bathymetry used in the model in *SS:peaks* and to the GEBCO bathymetry in *GEBCO:peaks*. First, we determine points that are local maxima in some direction using a 1D peak finding algorithm in each of the compass directions NS (& SN), WE (& EW), NW-SE (& SE-NW) and NE-SW (& SW-NE). We then filter this set of peaks to include only those that have a maximum in the direction of the local flow, defined by the bottom 500 m averaged velocity.

For each of these peaks, we define the width W_{full} as twice the minimum horizontal distance between the peak and the two bounding topographic minima along the flow direction, and the height H_{full} as minimum difference in topographic height between the peak and the bounding minima. We then approximate this feature locally as a 1D Gaussian bump of the form

$$h_{full}(x) = H_{full} e^{-\frac{x^2}{\beta^2 W_{full}^2}} \tag{C1}$$

where $\beta = 0.3$ is a Gaussian width scale, set so that the width of the base of a Gaussian is defined at 5% of its height.

We then calculate the maximum effective height $H_{max} = Fr_c|\mathbf{U}|/N$ (for some $Fr_C \sim O(1)$) to decide whether the flow will be blocked or not.

The new bump height H and width W are given by

$$H = \begin{cases} H_{full}, & H_{full} < H_{max} \\ H_{max}, & H_{full} \geq H_{max} \end{cases} \tag{C2}$$

$$W = \begin{cases} W_{full}, & \left(1 - e^{-\frac{1}{4\beta^2}}\right) H_{full} < H_{max} \\ 2\beta W_{full}\sqrt{-\ln\left(1 - H_{max}/H_{full}\right)}, & \left(1 - e^{-\frac{1}{4\beta^2}}\right) H_{full} \geq H_{max} \end{cases} \tag{C3}$$

$$\tag{C4}$$

where $1 - e^{-\frac{1}{4\beta^2}} \simeq 0.95$ is a correction associated with the estimate of the basal width of the Gaussian at 5% of its height.

The total energy flux associated with this peak can now be found, assuming the Gaussian shape. However, the 1D nature of this calculation must be corrected for. Suppose there is some isolated bathymetric feature given by $h(x,y)$, with Fourier transform $\tilde{h}(k,y)$ in x only, and $\hat{h}(k,l)$ in both x and y. Then supposing without loss of generality that the local flow is in the x direction, the total energy flux associated with this feature is (with reference to Eq. (3)):

$$E_{2D} = \frac{\rho_0 U}{2\pi^2}\int_{-\infty}^{\infty}\int_{|f/U|}^{|N/U|} |\hat{h}(k,l)|^2 \frac{|k|}{|\mathbf{k}|}\sqrt{(N^2 - \alpha U^2 k^2)(U^2k^2 - f^2)}\, dk\, dl\,, \tag{C5}$$

However, when estimating the generation, we are approximating this by an integral in y over individual 1D sections:

$$E_{1D} = \int_{-\infty}^{\infty} \frac{\rho_0 U}{\pi}\int_{|f/U|}^{|N/U|} \gamma(k)|\tilde{h}(k,y)|^2\sqrt{(N^2 - \alpha U^2 k^2)(U^2k^2 - f^2)}\, dk\, dy\,, \tag{C6}$$

$$= \frac{\rho_0 U}{2\pi^2}\int_{-\infty}^{\infty}\int_{|f/U|}^{|N/U|} \gamma(k)|\hat{h}(k,l)|^2\sqrt{(N^2 - \alpha U^2 k^2)(U^2k^2 - f^2)}\, dk\, dl\,, \tag{C7}$$

where $\gamma(k)$ is a correction factor so that $E_{1D} = E_{2D}$, and is given by:

$$\gamma(k) = \frac{\int_{-\infty}^{\infty} \frac{|k|}{|\mathbf{k}|}|\hat{h}(k,l)|^2\, dl}{\int_{-\infty}^{\infty} |\hat{h}(k,l)|^2\, dl} \tag{C8}$$

We have assumed for each y that $h(x,y)$ can be represented by a Gaussian. If we further assume that h is Gaussian in y with some horizontal lengthscale a, we obtain:

$$\gamma(k) = \frac{a|k|}{2\sqrt{\pi}}\int_{-\infty}^{\infty}(k^2 + l^2)^{-\frac{1}{2}} e^{-\frac{l^2a^2}{2}}\, dl \tag{C9}$$

$$= \frac{a|k|}{\sqrt{2\pi}} e^{\frac{k^2a^2}{4}} K_0\left(\frac{k^2a^2}{4}\right) \tag{C10}$$

where K_0 is the modified Bessel function of the second kind. As $|z| \to \infty$, $K_0(z) \to \sqrt{\frac{\pi}{2z}}e^{-z}\left(1 + \mathcal{O}\left(\frac{1}{z}\right)\right)$, thus as $a|k| \to \infty$ (topography becomes more 2D, or ridge-like), $\gamma(k) \to 1$.

We then assume that the topography is isotropic so that $a = W$, and use $\gamma(k)$ in our 2D expression for the energy flux of each section:

$$E_{sec} = \frac{\rho_0 U}{\pi}\int_{|f/U|}^{|N/U|} \gamma(k)|\tilde{h}(k,y)|^2\sqrt{(N^2 - \alpha U^2 k^2)(U^2k^2 - f^2)}\, dk \tag{C11}$$

The factor $\gamma(k)$ reduces the energy generation from a 3D obstacle compared to a 2D one. However, the aspect ratio of the relevant topographic feature is not calculable from this 1D section approach. This partial isotropy assumption is therefore a drawback of this method - the method is only exact for a small amplitude, isotropic Gaussian topography.

For each peak, the total energy flux is assumed to be distributed over a 20 km section parallel to the local flow and centred on the peak. Maps of energy flux, such as figures 11b-f are constructed by summing these sections for all peaks. Note that the total energy flux calculation is not dependent on this choice of 20 km, but spatial maps are. Maps of blocked height, width, and other parameters, can be constructed similarly, though instead of summing, the 'blocked height' at some point (if non-zero), is given as the blocked height associated with the most energetic lee wave with a section overlapping that point.

Open Research

All codes and processed data required to enable the reader to reproduce our results are available at https://doi:10.5281/zenodo.6659507 (Baker & Mashayek, 2022). Raw simulation data will be made available upon request to the authors.

Acknowledgments

L.B. was supported by the Centre for Doctoral Training in Mathematics of Planet Earth, UK EPSRC funded (grant no. EP/L016613/1), and A.M. acknowledges funding from the NERC IRF fellowship grant NE/P018319/1. GEBCO bathymetric data were provided by the GEBCO Bathymetric Compilation Group (2021). We would like to thank John Goff for providing access to the Goff (2010) abyssal hill dataset.

References

Alford, M. H., MacKinnon, J. A., Simmons, H. L., & Nash, J. D. (2016). Near-Inertial Internal Gravity Waves in the Ocean. *Ann. Rev. Mar. Sci.*, *8*(1), 95–123. doi: 10.1146/annurev-marine-010814-015746

Arbic, B. B. K., Fringer, O. B., Klymak, J. M., Mayer, F. T., & Trossman, D. S. (2019). Connecting process models of topographic wave drag to global eddying general circulation models. *Oceanography*, *32*(4), 146–155. doi: https://doi.org/10.5670/oceanog.2019.420.

Baines, P. G. (1995). *Topographic effects in stratified flows.* Cambridge: Cambridge University Press.

Baker, L. E., & Mashayek, A. (2021). Surface reflection of bottom generated oceanic lee waves. *J. Fluid Mech.*, *924, A17*. doi: 10.1017/jfm.2021.627

Baker, L. E., & Mashayek, A. (2022). *The impact of realistic topographic representation on the parameterisation of oceanic lee wave energy flux - software and data.* Zenodo. doi: 10.5281/zenodo.6659507

Bell, T. H. (1975). Topographically generated internal waves in the open ocean. *J. Geophys. Res.*, *80*(3), 320–327. Retrieved from `http://doi.wiley.com/10.1029/JC080i003p00320` doi: 10.1029/JC080i003p00320

Bretherton, F. P. (1969). Momentum transport by gravity waves. *Q. J. R. Meteorol. Soc.*, *95*, 125–135.

Broadbridge, M. B., Naveira Garabato, A. C., & Nurser, A. J. (2016, aug). Forcing of the overturning circulation across a circumpolar channel by internal wave breaking. *J. Geophys. Res. Ocean.*, *121*(8), 5436–5451. doi: 10.1002/2015JC011597

Chalamalla, V. K., & Sarkar, S. (2015). Mixing, dissipation rate, and their overturn-based estimates in a near-bottom turbulent flow driven by internal tides. *J. Phys. Oceanogr.*, *45*(8), 1969–1987. doi: 10.1175/JPO-D-14-0057.1

Cusack, J. M., Naveira Garabato, A. C., Smeed, D. A., & Girton, J. B. (2017). Observation of a Large Lee Wave in the Drake Passage. *J. Phys. Oceanogr.*, *47*(4), 793–810. Retrieved from http://journals.ametsoc.org/doi/10.1175/JPO-D-16-0153.1 doi: 10.1175/JPO-D-16-0153.1

de Marez, C., Lahaye, N. J., & Gula, J. (2020). Interaction of the Gulf Stream with small scale topography: a focus on lee waves. *Sci. Rep.*, *10*. Retrieved from www.nature.com/scientificreports doi: 10.1038/s41598-020-59297-5

Durran, D. R. (1986). Another Look at Downslope Windstorms. Part I: The Development of Analogs to Supercritical Flow in an Infinitely Deep, Continuously Stratified Fluid. *J. Atmos. Sci.*, *43*(21), 2527–2543.

Eckermann, S. D., Broutman, J. L., Ma, J., & Boybeyi, Z. (2010). Momentum fluxes of gravity waves generated by variable froude number flow over three-dimensional obstacles. *J. Atmos. Sci.*, *67*(7), 2260–2278. doi: 10.1175/2010JAS3375.1

Eliassen, A., & Palm, E. (1960). On the Transfer of Energy in Stationary Mountain Waves. *Geophys. Nor.*, *XXII*(3), 1–23.

Elvidge, A. D., Sandu, I., Wedi, N., Vosper, S. B., Zadra, A., Boussetta, S., ... Ujiie, M. (2019). Uncertainty in the Representation of Orography in Weather and Climate Models and Implications for Parameterized Drag. *J. Adv. Model. Earth Syst.*, *11*(8), 2567–2585. doi: 10.1029/2019MS001661

Epifanio, C. C., & Durran, D. R. (2001). Three-dimensional effects in high-drag-state flows over longridges. *J. Atmos. Sci.*, *58*(9), 1051–1065. doi: 10.1175/1520-0469(2001)058⟨1051:TDEIHD⟩2.0.CO;2

Forget, G. (2010, jun). Mapping ocean observations in a dynamical framework: A 2004-06 ocean atlas. *J. Phys. Oceanogr.*, *40*(6), 1201–1221. doi: 10.1175/2009JPO4043.1

Fox-Kemper, B., & Menemenlis, D. (2008). Can large eddy simulation techniques improve mesoscale rich ocean models? *Geophys. Monogr. Ser.*, *177*, 319–337. doi: 10.1029/177GM19

Gabor, D. (1946). Theory of Communication. *J. Inst. Electr. Eng.*, *93*(3), 429–457.

Garner, S. T. (2005). A topographic drag closure built on an analytical base flux. *J. Atmos. Sci.*, *62*(7 I), 2302–2315. doi: 10.1175/JAS3496.1

GEBCO Bathymetric Compilation Group. (2021). *GEBCO 2021 Grid.* doi: 10.5285/c6612cbe-50b3-0cff-e053-6c86abc09f8f

Goff, J. A. (2010). Global prediction of abyssal hill root-mean-square heights from small-scale altimetric gravity variability. *J. Geophys. Res. Solid Earth*, *115*(12), 1–16. doi: 10.1029/2010JB007867

Goff, J. A. (2020). Identifying Characteristic and Anomalous Mantle From the Complex Relationship Between Abyssal Hill Roughness and Spreading Rates. *Geophys. Res. Lett.*, *47*(11), 1–9. doi: 10.1029/2020GL088162

Goff, J. A., & Arbic, B. K. (2010, jan). Global prediction of abyssal hill roughness statistics for use in ocean models from digital maps of paleo-spreading rate, paleo-ridge orientation, and sediment thickness. *Ocean Model.*, *32*(1-2), 36–43. Retrieved from https://www.sciencedirect.com/science/article/pii/S1463500309001838 doi: 10.1016/j.ocemod.2009.10.001

Goff, J. A., & Jordan, T. H. (1988). Stochastic Modeling of Seafloor Morphology. *J. Geophys. Res.*, *93*.

Hogg, N. G. (1973). On the stratified Taylor column. *J. Fluid Mech.*, *58*(3), 517–537. doi: 10.1017/S0022112073002302

Klymak, J. M. (2018). Nonpropagating form drag and turbulence due to stratified flow over large-scale Abyssal Hill Topography. *J. Phys. Oceanogr.*, *48*(10), 2383–2395. doi: 10.1175/JPO-D-17-0225.1

Klymak, J. M., & Legg, S. M. (2010). A simple mixing scheme for models that resolve breaking internal waves. *Ocean Model.*, *33*(3-4), 224–234. Retrieved from http://dx.doi.org/10.1016/j.ocemod.2010.02.005 doi: 10.1016/j.ocemod.2010.02.005

Klymak, J. M., Legg, S. M., & Pinkel, R. (2010). High-mode stationary waves in

stratified flow over large obstacles. *J. Fluid Mech.*, *644*, 321–336. doi: 10.1017/S0022112009992503
Kunze, E., & Lien, R.-C. (2019). Energy Sinks for Lee Waves in Shear Flow. *J. Phys. Oceanogr.*, 2851–2865. doi: 10.1175/jpo-d-19-0052.1
Large, W. G., McWilliams, J. C., & Doney, S. C. (1994). Oceanic vertical mixing: A review and a model with a nonlocal boundary layer parameterization. *Rev. Geophys.*, *32*(4), 363–403. doi: 10.1029/94RG01872
Legg, S. (2021). Annual Review of Fluid Mechanics Mixing by Oceanic Lee Waves. *Annu. Rev. Fluid Mech.*, *53*, 173–201. doi: https://doi.org/10.1146/annurev-fluid-051220-043904
Leith, C. E. (1996). Stochastic models of chaotic systems. *Phys. D Nonlinear Phenom.*, *98*(2-4), 481–491. doi: 10.1016/0167-2789(96)00107-8
Lott, F. (1998). Linear mountain drag and averaged pseudo-momentum flux profiles in the presence of trapped lee waves. *Tellus, Ser. A Dyn. Meteorol. Oceanogr.*, *50*(1), 12–25. doi: 10.3402/tellusa.v50i1.14509
MacKinnon, J. A., Zhao, Z., Whalen, C. B., Griffies, S. M., Sun, O. M., Barna, A., … Norton, N. J. (2017). Climate Process Team on Internal Wave–Driven Ocean Mixing. *Bull. Am. Meteorol. Soc.*, *98*(11), 2429–2454. doi: 10.1175/bams-d-16-0030.1
Mashayek, A., Ferrari, R., Merrifield, S., Ledwell, J. R., St Laurent, L., & Garabato, A. N. (2017). Topographic enhancement of vertical turbulent mixing in the Southern Ocean. *Nat. Commun.*, *8*, 1–12. doi: 10.1038/ncomms14197
Mashayek, A., Salehipour, H., Bouffard, D., Caulfield, C. P., Ferrari, R., Nikurashin, M., … Caulfield, C. P. (2017). Efficiency of turbulent mixing in the abyssal ocean circulation. *Geophys. Res. Lett.*, *44*(12), 6296–6306. doi: 10.1002/2016gl072452
Mayer, F. T., & Fringer, O. B. (2017). An unambiguous definition of the Froude number for lee waves in the deep ocean. *J. Fluid Mech.*, *831*, 1–9. Retrieved from `https://doi.org/10.1017/jfm.2017.701` doi: 10.1017/jfm.2017.701
Mayer, F. T., & Fringer, O. B. (2020). Improving Nonlinear and Nonhydrostatic Ocean Lee Wave Drag Parameterizations. *J. Phys. Oceanogr.*, *50*(9), 2417–2435. doi: 10.1175/jpo-d-20-0070.1
Mayer, L., Jakobsson, M., Allen, G., Dorschel, B., Falconer, R., Ferrini, V., … Weatherall, P. (2018). The Nippon Foundation-GEBCO seabed 2030 project: The quest to see the world's oceans completely mapped by 2030. *Geosci.*, *8*(2). doi: 10.3390/geosciences8020063
Melet, A., Hallberg, R., Legg, S., Nikurashin, M., Melet, A., Hallberg, R., … Nikurashin, M. (2014, mar). Sensitivity of the Ocean State to Lee Wave–Driven Mixing. *J. Phys. Oceanogr.*, *44*(3), 900–921. Retrieved from `http://journals.ametsoc.org/doi/abs/10.1175/JPO-D-13-072.1` doi: 10.1175/JPO-D-13-072.1
Meredith, M. P., Meijers, A. S., Naveira Garabato, A. C., Brown, P. J., Venables, H. J., Abrahamsen, E. P., … Messias, M.-J. (2015). Circulation, retention, and mixing of waters within the Weddell-Scotia Confluence, Southern Ocean: The role of stratified Taylor columns. *J. Geophys. Res. Ocean.*, *120*, 547–562.
Merrifield, S. T., Laurent, L. S., Owens, B., Thurnherr, A. M., & Toole, J. M. (2016). Enhanced diapycnal diffusivity in intrusive regions of the Drake passage. *J. Phys. Oceanogr.*, *46*(4), 1309–1321. doi: 10.1175/JPO-D-15-0068.1
Miles, J. W., & Huppert, H. E. (1969). Lee waves in a stratified flow. Part 2. Semi-circular obstacle. *J. Fluid Mech.*, *33*(04), 803. doi: 10.1017/s0022112068001680
Naveira Garabato, A. C., Nurser, A. J. G., Scott, R. B., & Goff, J. A. (2013). The Impact of Small-Scale Topography on the Dynamical Balance of the Ocean. *J. Phys. Oceanogr.*, *43*. Retrieved from `https://journals.ametsoc.org/doi/pdf/10.1175/JPO-D-12-056.1` doi: 10.1175/JPO-D-12-056.1

Nikurashin, M., & Ferrari, R. (2010a). Radiation and Dissipation of Internal Waves Generated by Geostrophic Motions Impinging on Small-Scale Topography: Application to the Southern Ocean. *J. Phys. Oceanogr.*, *40*(9), 2025–2042. Retrieved from http://journals.ametsoc.org/doi/abs/10.1175/2010JPO4315.1https://journals.ametsoc.org/doi/pdf/10.1175/2009JPO4199.1https://journals.ametsoc.org/doi/pdf/10.1175/2010JPO4315.1 doi: 10.1175/2010jpo4315.1

Nikurashin, M., & Ferrari, R. (2010b). Radiation and dissipation of internal waves generated by geostrophic motions impinging on small-scale topography: Theory. *J. Phys. Oceanogr.*, *40*(5), 1055–1074. doi: 10.1175/2009JPO4199.1

Nikurashin, M., & Ferrari, R. (2011). Global energy conversion rate from geostrophic flows into internal lee waves in the deep ocean. *Geophys. Res. Lett.*, *38*(8), 1–6. doi: 10.1029/2011GL046576

Nikurashin, M., & Ferrari, R. (2013). Overturning circulation driven by breaking internal waves in the deep ocean. *Geophys. Res. Lett.*, *40*(12), 3133–3137. doi: 10.1002/grl.50542

Nikurashin, M., Ferrari, R., Grisouard, N., & Polzin, K. (2014). The Impact of Finite-Amplitude Bottom Topography on Internal Wave Generation in the Southern Ocean. *J. Phys. Oceanogr.*, *44*(11), 2938–2950. Retrieved from https://sites.physics.utoronto.ca/nicolasgrisouard/images/papers/2014_JPO_NikurashinFGP.pdf doi: 10.1175/jpo-d-13-0201.1

Nikurashin, M., Vallis, G. K., & Adcroft, A. (2012, jan). Routes to energy dissipation for geostrophic flows in the Southern Ocean. *Nat. Geosci.*, *6*(1), 48–51. Retrieved from http://www.nature.com/articles/ngeo1657 doi: 10.1038/ngeo1657

Peltier, W., & Clark, T. (1979). The Evolution and Stability of Finite-Amplitude Mountain Waves. Part II: Surface Wave Drag and Severe Downslope Windstorms. *J. Atmos. Sci.*, *36*(9), 1498–1529. doi: 10.1175/1520-0469(1980)037⟨2119:COEASO⟩2.0.CO;2

Perfect, B., Kumar, N., & Riley, J. J. (2020). Energetics of Seamount Wakes. Part II: Wave Fluxes. *J. Phys. Oceanogr.*, *50*(5), 1383–1398. doi: 10.1175/jpo-d-19-0104.1

Queney, P. (1948). The Problem of Air Flow Over Mountains: A Summary of Theoretical Studies. *Bull. Am. Meteorol. Soc.*, *29*(1), 16–26. doi: 10.1175/1520-0477-29.1.16

Scott, R. B., Goff, J. A., Naveira Garabato, A. C., & Nurser, A. J. G. (2011). Global rate and spectral characteristics of internal gravity wave generation by geostrophic flow over topography. *J. Geophys. Res.*, *116*(C09029), 1–14. doi: doi:10.1029/2011JC007005

Shakespeare, C. J. (2020). Interdependence of internal tide and lee wave generation at abyssal hills: Global calculations. *J. Phys. Oceanogr.*, *50*(3), 655–677. doi: 10.1175/JPO-D-19-0179.1

Shakespeare, C. J., Gibson, A. H., Hogg, A. M., Bachman, S. D., Keating, S. R., & Velzeboer, N. (2021). A New Open Source Implementation of Lagrangian Filtering: A Method to Identify Internal Waves in High-Resolution Simulations. *J. Adv. Model. Earth Syst.*, *13*(10). doi: 10.1029/2021ms002616

Shakespeare, C. J., & Hogg, A. M. C. (2017). The viscous lee wave problem and its implications for ocean modelling. *Ocean Model.*, *113*, 22–29. doi: 10.1016/j.ocemod.2017.03.006

Sheen, K. L., Brearley, J. A., Naveira Garabato, A. C., Smeed, D. A., Waterman, S., Ledwell, J. R., ... Watson, A. J. (2013). Rates and mechanisms of turbulent dissipation and mixing in the Southern Ocean: Results from the Diapycnal and Isopycnal Mixing Experiment in the Southern Ocean (DIMES). *J. Geophys. Res. Ocean.*, *118*(6), 2774–2792. doi: 10.1002/jgrc.20217

Simmons, A., Uppala, S., Dee, D., & Kobayashi, S. (2006). ERA-Interim: New

ECMWF reanalysis products from 1989 onwards. *ECMWF Newsl.*, *110*, 25–35. doi: doi:10.21957/pocnex23c6

Smith, & Sandwell, D. T. (1997). Global sea floor topography from satellite altimetry and ship depth soundings. *Science (80-.).*, *277*(5334), 1956–1962. doi: 10.1126/science.277.5334.1956

Smith, R. B. (1989). Mountain-induced stagnation points in hydrostatic flow. *Tellus A*, *41 A*(3), 270–274. doi: 10.1111/j.1600-0870.1989.tb00381.x

Smith, R. B. (2019). 100 Years of Progress on Mountain Meteorology Research. *Meteorol. Monogr.*, *59*, 1–73. doi: 10.1175/AMSMONOGRAPHS-D-18-0022.1

Smith, R. B., & Kruse, C. G. (2018). A gravity wave drag matrix for complex terrain. *J. Atmos. Sci.*, *75*(8), 2599–2613. doi: 10.1175/JAS-D-17-0380.1

St. Laurent, L., Naveira Garabato, A. C., Ledwell, J. R., Thurnherr, A. M., Toole, J. M., & Watson, A. J. (2012). Turbulence and diapycnal mixing in drake passage. *J. Phys. Oceanogr.*, *42*(12), 2143–2152. doi: 10.1175/JPO-D-12-027.1

Taylor, G. I. (1923). Stability of a Viscous Liquid Contained between Two Rotating Cylinders. *Philos. Trans. R. Soc. A Math. Phys. Eng. Sci.*, *223*(605-615), 289–343. doi: 10.1098/rsta.1923.0008

Teixeira, M. A. (2014). The physics of orographic gravity wave drag. *Front. Phys.*, *2*, 1–24. doi: 10.3389/fphy.2014.00043

Tozer, B., Sandwell, D. T., Smith, W. H., Olson, C., Beale, J. R., & Wessel, P. (2019). Global Bathymetry and Topography at 15 Arc Sec: SRTM15+. *Earth Sp. Sci.*, *6*(10), 1847–1864. doi: 10.1029/2019EA000658

Trossman, D. S., Arbic, B. K., Garner, S. T., Goff, J. A., Jayne, S. R., Metzger, E. J., & Wallcraft, A. J. (2013). Impact of parameterized lee wave drag on the energy budget of an eddying global ocean model. *Ocean Model.*, *72*, 119–142.

Trossman, D. S., Waterman, S., Polzin, K. L., Arbic, B. K., Garner, S. T., Naveira Garabato, A. C., & Sheen, K. L. (2015). Internal lee wave closures: Parameter sensitivity and comparison to observations. *J. Geophys. Res. Ocean.*, 2813–2825. doi: 10.1002/2014JC010387.Received

Tulloch, R., Ferrari, R., Jahn, O., Klocker, A., Lacasce, J., Ledwell, J. R., ... Watson, A. (2014). Direct estimate of lateral eddy diffusivity upstream of drake passage. *J. Phys. Oceanogr.*, *44*(10), 2593–2616. doi: 10.1175/JPO-D-13-0120.1

Voet, G., Alford, M. H., MacKinnon, J. A., & Nash, J. D. (2020). Topographic Form Drag on Tides and Low-Frequency Flow: Observations of Nonlinear Lee Waves over a Tall Submarine Ridge near Palau. *J. Phys. Oceanogr.*, 1489–1507. doi: 10.1175/jpo-d-19-0257.1

Voisin, B. (2007). Lee waves from a sphere in a stratified flow. *J. Fluid Mech.*, *574*, 273–315. doi: 10.1017/S0022112006004095

Vosper, S. B., Brown, A. R., & Webster, S. (2016). Orographic drag on islands in the NWP mountain grey zone. *Q. J. R. Meteorol. Soc.*, *142*(701), 3128–3137. doi: 10.1002/qj.2894

Vosper, S. B., van Niekerk, A., Elvidge, A., Sandu, I., & Beljaars, A. (2020). What can we learn about orographic drag parametrisation from high-resolution models? A case study over the Rocky Mountains. *Q. J. R. Meteorol. Soc.*, *146*(727), 979–995. doi: 10.1002/qj.3720

Waterman, S., Naveira Garabato, A. C., & Polzin, K. L. (2013). Internal waves and turbulence in the antarctic circumpolar current. *J. Phys. Oceanogr.*, *43*(2), 259–282. doi: 10.1175/JPO-D-11-0194.1

Waterman, S., Polzin, K. L., Garabato, A. C., Sheen, K. L., & Forryan, A. (2014). Suppression of internal wave breaking in the antarctic circumpolar current near topography. *J. Phys. Oceanogr.*, *44*(5), 1466–1492. doi: 10.1175/JPO-D-12-0154.1

Welch, W. T., Smolarkiewicz, P., Rotunno, R., & Boville, B. A. (2001). The large-scale effects of flow over periodic mesoscale topography. *J. Atmos. Sci.*, *58*(12), 1477–1492. doi: 10.1175/1520-0469(2001)058⟨1477:TLSEOF⟩2.0.CO;2

Whalen, C. B., de Lavergne, C., Naveira Garabato, A. C., Klymak, J. M., MacKinnon, J. A., & Sheen, K. L. (2020, nov). *Internal wave-driven mixing: governing processes and consequences for climate* (Vol. 1) (No. 11). Springer Nature. doi: 10.1038/s43017-020-0097-z

Wright, C. J., Scott, R. B., Ailliot, P., & Furnival, D. (2014). Lee wave generation rates in the deep ocean. *Geophys. Res. Lett.*, *41*(7), 2434–2440. doi: 10.1002/2013GL059087

Wunsch, C., & Ferrari, R. (2004). Vertical Mixing, Energy, and the General Circulation of the Oceans. *Annu. Rev. Fluid Mech.*, *36*(1), 281–314. Retrieved from `http://arjournals.annualreviews.org/doi/abs/10.1146%2Fannurev.fluid.36.050802.122121` doi: 10.1146/annurev.fluid.36.050802.122121

Wurtele, M. (1996). Atmospheric Lee Waves. *Annu. Rev. Fluid Mech.*, *28*(1), 429–476. doi: 10.1146/annurev.fluid.28.1.429

Yang, L., Nikurashin, M., Hogg, A. M., & Sloyan, B. M. (2018). Energy Loss from Transient Eddies due to Lee Wave Generation in the Southern Ocean. *J. Phys. Oceanogr.*, *48*(12), 2867–2885. Retrieved from `www.ametsoc.org/PUBSReuseLicenses` doi: 10.1175/jpo-d-18-0077.1

Zheng, K., & Nikurashin, M. (2019). Downstream Propagation and Remote Dissipation of Internal Waves in the Southern Ocean. *J. Phys. Oceanogr.*. Retrieved from `www.ametsoc.org/PUBSReuseLicenses` doi: 10.1175/JPO-D-18-0134.1

Zheng, K., Nikurashin, M., & Tian, J. (2022). Non-local energy dissipation of lee waves and turbulence in the South China Sea. *J. Geophys. Res. Ocean.*, 1–15. doi: 10.1029/2021jc017877